Aerodynamic model of counter-rotating coaxial rotors near the ground

Garofano-Soldado, Ambar; Ragni, Daniele; Pereira, Lourenço T.Lima; Zamponi, Riccardo; Ollero, Anibal; Heredia, Guillermo

DOI
10.1016/j.ast.2025.111112

Publication date
2026

Document Version
Final published version

Published in
Aerospace Science and Technology

Citation (APA)
Garofano-Soldado, A., Ragni, D., Pereira, L. T. L., Zamponi, R., Ollero, A., & Heredia, G. (2026). Aerodynamic model of counter-rotating coaxial rotors near the ground. *Aerospace Science and Technology*, *168*, Article 111112. https://doi.org/10.1016/j.ast.2025.111112

Aerospace Science and Technology 168 (2026) 111112

Contents lists available at ScienceDirect

Aerospace Science and Technology

journal homepage: www.elsevier.com/locate/aescte

Original article

Aerodynamic model of counter-rotating coaxial rotors near the ground

Ambar Garofano-Soldado [a,*], Daniele Ragni [b], Lourenço T. Lima Pereira [b], Riccardo Zamponi [b,c], Anibal Ollero [a], Guillermo Heredia [a]

[a] GRVC Robotics Lab Seville, University of Seville, Spain
[b] Department of Flow Physics and Technology, Delft University of Technology, Netherlands
[c] Department of Environmental and Applied Fluid Dynamics, von Karman Institute for Fluid Dynamics, Belgium

ARTICLE INFO

Communicated by Dr Bing Wang

Keywords:
Coaxial rotors
Ground effect
Aerodynamic model
Rotor spacing

ABSTRACT

This study focuses on the analysis of the ground effect in counter-rotating coaxial rotors. To investigate the aerodynamic performance of a coaxial rotor system, the aerodynamic loading is measured for different rotor vertical spacing, rotational speed, and height above the ground. To link aerodynamic loading with flow topology, velocity fields in the rotor slipstreams are measured with particle image velocimetry (PIV). A semi-empirical model is additionally proposed to complement existing ground-effect theories from the literature by accounting for the effects of rotor spacing, ground proximity, and rotor-to-rotor aerodynamic interactions. The results of the performance analysis show that the ground effect is more pronounced in coaxial configurations than in single rotors, especially at minimum spacing and height, where the thrust increases about twice the corresponding value of single rotors. The analysis of the PIV velocity fields reveals how the inflow to the bottom rotor accelerates the downstream flow, increasing the flow rate and further reducing the induced velocity near the ground. As the rotor spacing increases, these interactions weaken, causing the aerodynamic loading to converge to that of a single rotor at a spacing around 90 % of the rotor radius. The proposed model inspired by experimental data provides a robust framework for predicting coaxial rotor performance near the ground. It also allows integration of the ground effect model into UAV control strategies for improved flight stability and safety.

1. Introduction

The evolution of aerial vehicle technology has been driven by the pursuit of high performance, efficiency and adaptability across a wide range of operational environments. A central aspect of this progress has been the development of innovative rotor configurations tailored to specific mission profiles [1]. Among these, coaxial rotors were originally introduced in helicopters to counteract torque without the need for a tail rotor [2]. More recently, they have attracted considerable interest in unmanned aerial applications due to their favorable thrust-to-weight ratio, compact geometry, high stability, and increased lift. These characteristics make them particularly well suited for modern unmanned aerial vehicles (UAVs), with growing applications in urban air mobility (UAM), inspection, surveillance, and operations in confined or cluttered environments [3–6]. Recent advancements in rotorcraft design and control technology have further broadened the range of applications for coaxial systems [7], facilitating their integration into a new generation of UAV platforms.

Despite their practical advantages, coaxial rotors exhibit complex aerodynamic behavior, primarily due to the interaction between the slipstreams of the upper and lower rotors. This interaction is governed by parameters such as the axial rotor spacing and flight conditions, and can lead to significant variations in thrust generation and propulsive efficiency [8–11]. Ramasamy [10] quantified the change in performance of coaxial rotor systems with different rotor spacings under hovering conditions, revealing that, while the efficiency of the top rotor decreases with increasing separation, the opposite occurs for the bottom rotor. Shukla [12] observed that the combination of the top and bottom rotors forms a non-uniform wake distribution that varies with rotor spacing. Similarly, Ko et al. [11] showed that smaller axial rotor spacing affects wake dynamics, increasing blade-vortex interaction and overall flow instability. Their findings indicated that reducing the separation between the rotors intensifies wake interactions, resulting in pronounced asymmetry in the flow field, particularly in the bottom rotor, which is directly influenced by the wake of the top rotor. As a result, the aerodynamic performance of the rotors is significantly affected. Park et al. [13] supported these findings with a numerical analysis of a similar configuration in hovering and forward flight. Their results revealed opposite trends in the thrust coefficient of the bottom rotor depending on flight conditions. However, the total thrust remained relatively stable across

* Corresponding author.
E-mail address: agarofano@us.es (A. Garofano-Soldado).

https://doi.org/10.1016/j.ast.2025.111112
Received 2 April 2025; Received in revised form 2 September 2025; Accepted 16 October 2025
Available online 26 October 2025

Nomenclature

δv_{i_B}	Induced velocity of the bottom image rotor, m/s
δv_{i_T}	Induced velocity of the top image rotor, m/s
δv_i	Induced velocity of the image rotor, m/s
ν	Kinematic viscosity, m^2/s
$\dot{m}$	Mass flow rate, kg/s
Ω_B	Rotational speed in bottom rotor, RPM
Ω_T	Rotational speed in top rotor, RPM
ρ	Air density, kg/m^3
A	Rotor disk area, m^2
C_Q	Rotor torque coefficient
C_T	Rotor thrust coefficient
d	Rotor spacing, m
f_B	Induced velocity reduction factor in the bottom rotor
f_T	Induced velocity reduction factor in the top rotor
n	Number of rotors
Q	Rotor torque, Nm
R	Rotor radius, m
s_B	Strength of the bottom image source, m^3/s
s_T	Strength of the top image source, m^3/s
$T_{\mathrm{IGE_B}}$	In-Ground-Effect thrust in the bottom rotor, N
$T_{\mathrm{IGE_s}}$	In-Ground-Effect thrust in a single rotor, N
$T_{\mathrm{IGE_T}}$	In-Ground-Effect thrust in the top rotor, N
T_{IGE}	In-Ground-Effect total thrust, N
$T_{\mathrm{OGE_B}}$	Out-of-Ground-Effect thrust in the bottom rotor, N
$T_{\mathrm{OGE_s}}$	Out-of-Ground-Effect thrust in a single rotor, N
$T_{\mathrm{OGE_T}}$	Out-of-Ground-Effect thrust in the top rotor, N
T_{OGE}	Out-of-Ground-Effect total thrust, N
u, v	Velocity components, m/s
$v_{\mathrm{IGE_B}}$	Induced velocity in ground effect in the bottom rotor, m/s
$v_{\mathrm{OGE_T}}$	Induced velocity out of ground effect in the top rotor, m/s
v_{IGE}	Induced velocity in ground effect, m/s
V_{IN}	Inflow velocity, m/s
$v_{\mathrm{OGE_B}}$	Induced velocity out of ground effect in the bottom rotor, m/s
$v_{\mathrm{IGE_T}}$	Induced velocity in ground effect in the top rotor, m/s
v_{OGE}	Induced velocity out of ground effect, m/s
V_{OUT}	Outflow velocity, m/s
v_h	Hover induced velocity, m/s
z	Rotor-to-ground distance, m
Acronyms	
BVI	Blade-Vortex interaction
CCR	Counter-rotating coaxial rotors
IGE	In-Ground-Effect
OGE	Out-of-Ground-Effect
PIV	Particle Image Velocimetry
UAM	Urban Air Mobility
UAV	Unmanned Aerial Vehicles

different rotor spacings in both flight scenarios. Furthermore, Russo et al. [14] found that, when the rotor separation is equal to the rotor diameter, the performance of the upper and bottom rotors becomes nearly identical. This contrasts with the more pronounced effects observed in smaller rotor separations.

While the aerodynamic behavior of coaxial rotors in unbounded environments has been extensively studied, considerably less is known about how these interactions are affected when the system operates near solid boundaries, such as the ground plane. In these conditions, the flow generated by each rotor interacts with not only the other rotor but also the ground surface, modifying the inflow patterns and pressure distribution throughout the rotor system. The phenomenon, known as the ground effect, has been extensively studied for single rotors due to its significant influence on thrust generation [15]. For small-scale systems, thrust increases of up to 18 % have been reported when hovering close to the ground. This magnitude, though, depends on the rotor configuration [16] and the operating conditions [17]. The ground effect is typically quantified using aerodynamic models derived from theoretical formulations [18] or empirical data fitting [15]. Accurate modeling of this phenomenon is essential for predicting rotor performance and, ultimately, for enabling efficient control strategies in low-altitude flight or during takeoff and landing maneuvers [19,20]. However, while the ground effect for isolated rotors has been well characterized, its behavior in coaxial configurations is less well understood. The combined influence of rotor-rotor and rotor-ground interactions introduces additional aerodynamic complexity that is not fully described by the existing models.

Several recent studies have begun to address the interaction between coaxial rotors and proximity to the ground. In this context, Silwal et al. [21] experimentally investigated the ground effect in coaxial rotor systems by varying both the rotor height and the axial rotor spacing under controlled thrust conditions. The study included both trimmed conditions, where the collective pitch was adjusted to maintain constant thrust, and untrimmed conditions with fixed pitch. Their results showed that the overall ground effect remained largely unchanged across different rotor spacings and was comparable to that of a single rotor, under the consideration that the rotor height was defined relative to the midpoint between the upper and lower rotors. Similarly, Zhu et al. [22] explored how the ground effect varies in coaxial systems with fixed axial spacing but variable lateral separation. They observed a notable increase in thrust near the ground for coaxial configurations compared to the single-rotor case.

These studies, nevertheless, do not propose ground effect models capable of predicting the thrust behavior in coaxial configurations as a function of both rotor-to-ground distance and axial rotor spacing. This model is of fundamental relevance for the assessment of takeoff and landing performance of coaxial rotors. Classical formulations, such as the Cheeseman and Bennett theory [18], were developed for isolated rotors and do not incorporate axial separation as a parameter. In addition, the evolution of the flow field in coaxial rotors under near-ground conditions remains insufficiently understood, particularly when interactions between the rotors and nearby surfaces become significant. A deeper understanding of these aerodynamic interactions is essential to inform future control strategies. Such knowledge would enable UAVs to anticipate thrust variations caused by ground proximity and rotor spacing, and incorporate this information into onboard control systems. This could improve energy efficiency, flight stability, and safety, particularly during low-altitude maneuvers such as takeoff and landing, as demonstrated in previous studies in a quadcopter [19] and a fully-actuated hexarotor with tilted propellers [20].

To address this gap, this paper presents an experimental investigation of the ground effect in coaxial rotors, focusing on how thrust changes with the relative placement of the top and bottom rotors relative to the ground plane. The study examines the influence of the axial rotor spacing (d) and the height of the bottom rotor above the ground (z), using two custom-designed test benches: one for direct thrust measurement and another for flow field visualization. The thrust increase for each configuration is quantified, and a threshold is established where the ground effect of a single rotor becomes equivalent to that of two coaxial rotors. Aerodynamic interactions are further evaluated through a 2D flow pattern analysis using particle image velocimetry (PIV), providing insight into the wake topology near the ground and between the rotors. These findings reinforce the thrust ratio results and increase the understanding of physical mechanisms. Additionally, the effect of varying rotational speeds between the top and bottom rotors is examined, considering four configurations for each rotor. Finally, the study extends existing theoretical frameworks by proposing a novel ground effect model for coaxial rotors. This model incorporates the rotor spacing and ground distance and uses experimental data to account for

induced velocity variations caused by rotor interactions. Such modeling framework could be incorporated into future control architectures for coaxial UAVs, providing a predictive basis for managing aerodynamic effects in near-ground operations, consequently improving safety, precision, and reliability of operations of coaxial rotor systems.

2. Theory of rotors in ground effect

The proximity of a rotor to the ground modifies the development of slipstream contraction. Specifically, the presence of the ground plane reduces the induced velocity generated by the rotor, as illustrated in Fig. 1. As the rotor height decreases, the thrust increases under constant power conditions [23]. This phenomenon has been widely studied in the literature across various rotor configurations and operating conditions [15,16]. Similarly, when thrust is held constant, the power required decreases as the rotor moves closer to the ground [21]. In both scenarios, reduced rotor height improves aerodynamic performance due to attenuation of the induced flow. In the present work the constant-power assumption is adopted specifically for the derivation of the theoretical model, in line with established approaches in the literature [23]. Conventional terminology is used consistently in this manuscript: if the rotor is operating close to the ground, the produced thrust is referred to as in-ground-effect thrust (T_{IGE}), while the thrust generated outside the influence of the ground plane is denoted as out-of-ground-effect thrust (T_{OGE}). The ratio $T_{\mathrm{IGE}}/T_{\mathrm{OGE}}$ serves as a key metric to quantify the performance gains associated with proximity to the ground plane.

The ground effect has been extensively analyzed using different analytical approaches, the method of images being the most widely adopted due to its simplicity [15,23,24]. This approach consists of introducing a virtual image rotor below the ground plane to represent the non-penetration boundary condition at the surface. The most widely recognized formulation is from Cheeseman and Bennett [18]. In their model, the rotor is approximated by a potential flow source with strength $s = A\, v_i/4\pi$, where A is the rotor disk area and v_i is the induced velocity. Although simplified, this approach effectively captures key aspects of the influence of ground proximity on induced velocity and thrust performance. According to the power equation for a rotor that hovers in an unconfined space [23], the induced power is related to the rotor thrust (T) and the induced velocity according to $P_i = T\, v_i$. Assuming that the power remains constant, the rotor power can be expressed as

$$T_{\mathrm{IGEs}} \cdot v_{\mathrm{IGE}} = T_{\mathrm{OGEs}} \cdot v_{\mathrm{OGE}}, \tag{1}$$

where v_{IGE} and v_{OGE} denote the induced velocities under IGE and OGE conditions, respectively. The ground proximity reduces the induced velocity [18], leading to

$$v_{\mathrm{IGE}} = v_{\mathrm{OGE}} - \delta v_i. \tag{2}$$

Here, δv_i denotes the infinitesimal change in the induced velocity due to the proximity of the image rotor to the ground. Using the definition of a 3D potential source, the scalar potential field generated by the image rotor located at $\mathbf{r}_0 = (x_0, y_0, z_0)$ is given by

$$\phi(x, y, z) = -\frac{s}{\sqrt{(x - x_0)^2 + (y - y_0)^2 + (z - z_0)^2}}. \tag{3}$$

Consequently, the induced velocity δv_i is obtained by taking the gradient of the potential

$$\boldsymbol{\delta \mathbf{v}_i}(x, y, z) = \nabla \phi(x, y, z). \tag{4}$$

Only the z-component of the induced velocity is considered, since the rotor is located along the z-axis. As a result, the ground effect model can be expressed as

$$\left[\frac{T_{\mathrm{IGEs}}}{T_{\mathrm{OGEs}}}\right]_{(z)} = \frac{1}{1 - \dfrac{\delta v_i(z)}{v_{i\infty}}} = \frac{1}{1 - \left(\dfrac{R}{4z}\right)^2}, \tag{5}$$

where z is the rotor height above the ground, R is the rotor radius, and $v_{i\infty}$ corresponds to the induced velocity in OGE conditions (v_{OGE}). This formulation highlights that the ground effect is modeled as a change in the induced velocity or rotor thrust. In coaxial systems, the interaction between the rotors significantly alters the flow pattern. The induced velocity of each rotor is modified both by its interference with the other rotor and by its distance from the ground. Fig. 1 shows the coaxial arrangement and highlights essential parameters such as the bottom rotor height and the rotor spacing, typically normalized by the rotor radius. According to Ko and Lee [11], the distance d is a critical factor in the performance of coaxial configurations. Consequently, the combined effects of rotor height and axial rotor separation lead to variations in the ground effect compared to a single rotor, which does not experience incoming flow disturbances.

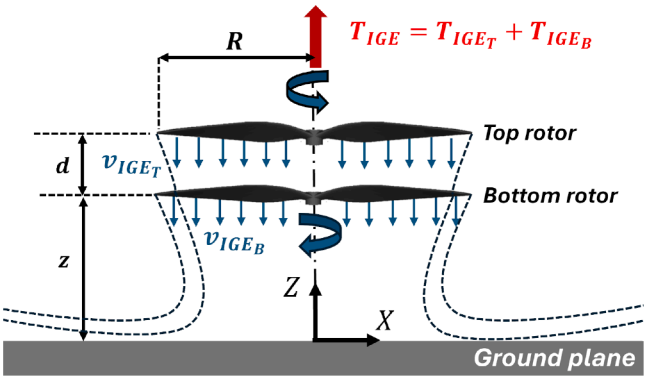

Fig. 1. Schematic of the counter-rotating coaxial rotor configuration. Key parameters, including the rotor spacing (d) and the distance to the ground (z), are indicated.

The present study aims to further extend the classical Cheeseman and Bennett model to account for variations in induced velocity in coaxial rotor systems. The proposed model incorporates both the rotor spacing (d) and the height above the ground (z) to provide a more accurate prediction of the ground effect in these configurations. In addition, following previous theories, these parameters are normalized to the rotor radius to obtain a dimensionless ground effect model.

3. Experimental setup

This section introduces the experimental setup, including a description of the coaxial configuration under analysis, the two custom-built test benches, and their respective operating conditions. Different measurement techniques are employed in each test system: force measurements to assess the rotor performance and PIV to characterize the flow field within the rotors. The tests are conducted at the Faculty of Aerospace Engineering of the Delft University of Technology.

3.1. Coaxial rotor configuration

Two counter-rotating coaxial rotors are placed perpendicular to the ground plane at varying heights and rotor spacings, sharing a common axis of rotation, as shown in Fig. 1. In addition, the single rotor configuration is analyzed to serve as a baseline for comparison with the coaxial system. The bottom rotor in the coaxial configuration, as well as the single rotor, is positioned at a distance z from the ground. This arrangement enables the analysis of the effects induced by the top rotor in each scenario and its influence on the thrust generation mechanisms. In both configurations, the selected rotors are two-blade plastic models manufactured by APC, each with a diameter of 381 mm and a pitch of 139.7 mm (APC 15x5.5). These rotors are commonly used in small UAV applications [1] and have previously been employed on the LARES octo-quad multi-rotor platform [25]. The chord and twist distributions along the rotor blade are shown in Fig. 2.

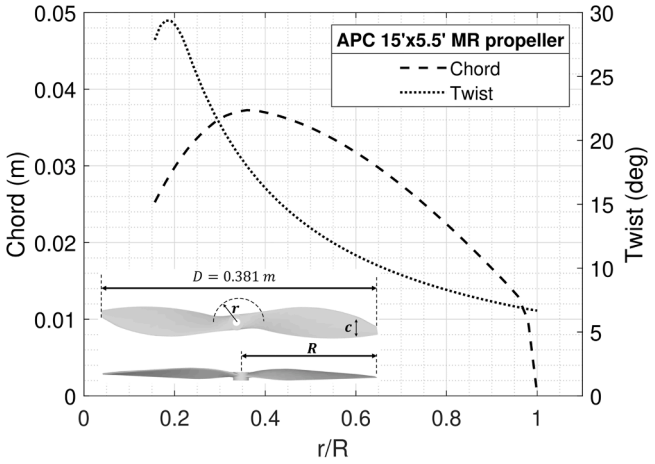

Fig. 2. Chord and twist distribution of the APC 15x5.5MR propeller.

Table 1
Overview of the operating conditions for the different analyses under study.

Parameter	Value
Number of blades	2
Rotor radius, R [mm]	190.5
Rotational speed, Ω [RPM]	3500, 4000, 4500
Reynold number, Re	0.90×10^5, 1.03×10^5, 1.16×10^5
Rotor-to-rotor spacing, d/R	0.18, 0.29, 0.4, 0.5, 0.9
Rotor-to-ground distance, z/R	0.5, 0.75, 1, 1.5, 2, 3
Tip Mach number, M_{tip}	0.20, 0.23, 0.26

Each rotor is driven by a T-Motor AT4130 450KV brushless DC motor, powered by a 5KW DC power supply. The motors are operated using HBC25063 controllers from the MGM COMPRO 120V series, specifically designed for high-performance and demanding applications. The control system integrates the National Instruments NI 9263 module, which enables real-time adjustment of throttle settings to achieve the desired rotor speed. The motors are controlled independently, ensuring precise speed adjustment. This analysis considers rotational speeds of 3500 RPM, 4000 RPM, and 4500 RPM, with Reynolds numbers ranging from 0.90×10^5 to 1.16×10^5, based on the blade sectional chord at 0.75R [26]. The range of rotor spacings includes $d/R = [0.18, 0.29, 0.4, 0.5, 0.9]$, while the distance from the ground plane is set at $z/R = [0.5, 0.75, 1, 1.5, 2, 3]$. Table 1 summarizes the experimental operating conditions.

3.2. Test bench and operating conditions

3.2.1. Force measurement

A balance system is employed to measure the aerodynamic forces generated by the counter-rotating coaxial rotors (CCR). The test bench, constructed from aluminum beams for enhanced rigidity and stability, has dimensions of 0.75 m × 1.5 m × 1 m, as illustrated in Fig. 3. This robust framework ensures precise alignment of components during testing, minimizing any structural deflections that could compromise measurement accuracy.

The experimental setup is designed to be both modular and reconfigurable, allowing for precise adjustment of key experimental parameters while minimizing aerodynamic interferences. As shown in Fig. 3, the rotors are positioned parallel to a vertical wall, which serves as a ground plane. This configuration minimizes any interference between the rotor wake and surrounding structural elements. Rotor spacing can be adjusted by shifting the top rotor along the two vertical aluminium beams, providing fine control over the relative positioning of the rotors. In addition, the rotor height relative to the ground plane can be varied by moving the entire structure. A calibrated six-component external balance (OJF External Balance B8604), provided by the Netherlands Aerospace Laboratory (NLR), is used to measure the forces acting on the entire rotor system. The rotors are mounted on a rigid structure that is directly connected to the balance, allowing the total forces to be measured on the set of coaxial rotors rather than on each rotor individually. The balance is able to measure forces and moments within a maximum nominal load range of ±500 N for axial and side forces and up to ±500 N m for the rolling moment. For more detailed information on external balance, the reader is referred to the NLR report [27].

Table 2
Operating conditions for force measurements in the coaxial configuration. Analysis 1 examines the influence of rotational speed of each rotor, while Analysis 2 explores the effect of rotor separation.

Parameter	Analysis 1	Analysis 2
Rotational speed, Ω [RPM]	0, 3500, 4000, 4500	4000
Rotor-to-rotor spacing, d/R	0.9	0.18, 0.29, 0.4, 0.5, 0.9
Rotor-to-ground distance, z/R	0.5, 0.75, 1, 1.5, 2, 3	0.5, 0.75, 1, 1.5, 2, 3

The first part of the study examines the impact of varying the rotational speed of the rotors while keeping the rotor spacing fixed at $d = 0.9\,R$. The objective is to investigate how the ground effect changes when the speed of the top rotor differs from that of the bottom rotor. In this approach, the speed of one rotor is kept constant while the speed of the other is varied from 0 RPM to 4500 RPM. The experiments are then repeated for six different ground distances, ensuring a comprehensive examination of the ground effect over a range of speeds and heights. The second study analyses the effect of the rotor spacing on ground proximity. A constant rotational speed of 4000 RPM is maintained for both rotors and five different rotor spacings are tested. A total of 30 experiments are conducted using the same rotor-to-ground distances as in the first study. Table 2 provides an overview of the operating conditions for each analysis.

All tests are conducted using a fixed input voltage to ensure consistency across experiments. Data acquisition of the force measurements is carried out with LabVIEW. Data are recorded after an initial 20 s buffer period with the motors off to obtain zero-balance readings. Following this, a controlled ramp-up is performed to gradually accelerate the motor to the target rotational speed. The system typically stabilizes within approximately 10 s. Once steady-state conditions are reached, measurements are collected over a 40 s interval, resulting in a total of approximately 80,000 samples (2,000 samples per second). The mean thrust during this period is then calculated and used as a representative value for the test. It should be noted that only thrust was measured in this study, as torque acquisition was beyond the capabilities of the experimental setup and lay outside the scope of the investigation. To assess the variability of the system, the time series is segmented into intervals corresponding to 50 motor revolutions (to reduce the effect of periodic variations of force due to asymmetries from the setup), and the mean thrust is computed for each segment. This analysis is performed independently for each configuration evaluated in the study. The resulting standard deviation reached a maximum of 0.11 N in the mean thrust measurements. When error propagation is applied to evaluate the ground effect ratio (T_{IGE}/T_{OGE}), the maximum relative error observed is 1.7 %, occurring at the largest distance from the ground plane (3R). These uncertainties are attributed to a combination of experimental factors, including intrinsic structural vibrations, slight variations in motor positioning, and other sources of error inherent to the experimental setup. Despite these sources of uncertainty, the relatively low magnitude of standard deviations supports the accuracy and repeatability of the measurement procedure.

The performance of the rotor is first validated under static and unconfined conditions. Fig. 4 illustrates both the thrust coefficient, C_T, defined as $C_T = T/(\rho A\Omega^2 R^2)$, and the torque coefficient, C_Q, expressed as $C_Q = Q/(\rho A\Omega^2 R^3)$, plotted against the rotational speed in RPM. The close agreement between the experimental results and the

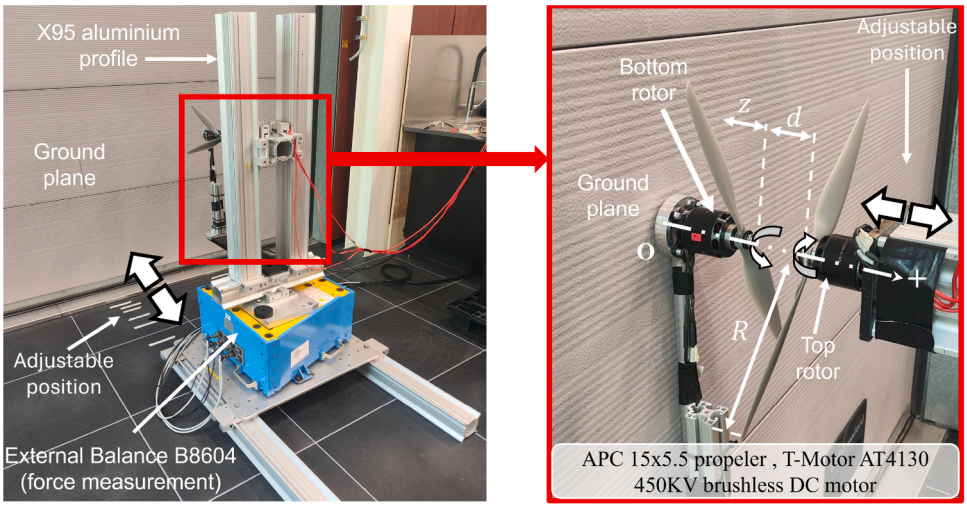

Fig. 3. Test bench designed to evaluate the ground effect on a set of coaxial rotors under varying operating conditions. Different axial rotor spacing and distances from the wall are considered to quantify the thrust increase for each configuration. This experimental setup is also used to evaluate a single propeller at different heights.

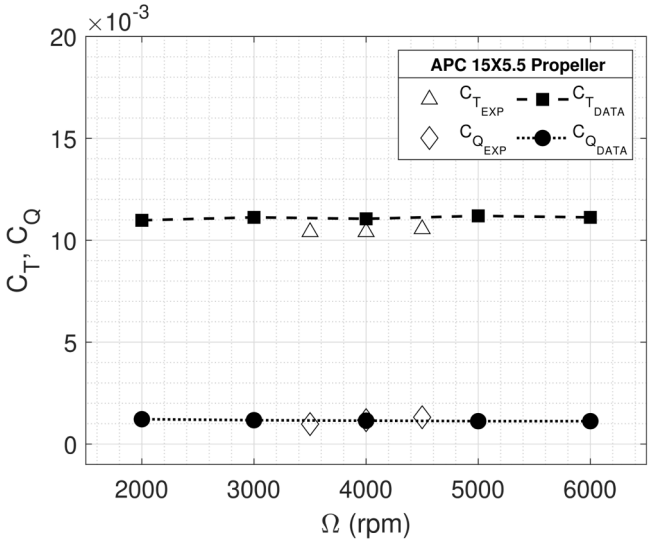

Fig. 4. Static performance of the 15x5.5MR APC propeller at different rotational speeds. Comparison of the thrust and torque coefficients between experimental data and manufacturer data.

manufacturer's reference data highlights the reliability of the experimental setup and the robustness of the measurement procedures.

3.2.2. Particle image velocimetry

Stereoscopic PIV measurements were performed to investigate the flow field in the z-x plane, as shown in Fig. 5. The measurement plane was oriented normal to the ground, intersecting the rotation axis of the propellers. The imaging system consisted of two Imager sCMOS cameras (LaVision GmbH, sensor size of 2560px × 2160px, pixel size of 6.5 µm × 6.5 µm), which were placed to achieve a solid viewing angle of approximately 32°, as shown in Fig. 5. The camera perpendicular to the measurement plane was equipped with a Nikon 35mm lens, set to an f-number of 11. The second camera imaged the field of interest through a Nikon 50mm lens with an f-number of 8. For the latter, the combination of focal length and f-number was selected to account for the variation in working distance with respect to the first camera and the back-scattering effect. In addition, a Scheimpflug adapter was installed on the second camera to improve image quality. A printed calibration plate with a grid of black dots was used for the image calibration. Following Wieneke [28], self-calibration was carried out in DaVis 10.2 (LaVision GmbH) to map the images. The calibration used a pinhole model to dewarp the images in a final field of view of 2772px × 2108px (420mm × 320mm) with a digital resolution of 6.6px/mm.

Table 3
Operating conditions for PIV measurements in the coaxial rotor configuration.

Parameter	Value
Image rate [Hz]	15
Acquisition sensor [px]	2560 × 2160
Interrogation window [px]	16 × 16
Overlap factor [%]	75
Rotational speed, Ω [RPM]	4000
Rotor-to-rotor spacing, d/R	0.18, 0.29
Rotor-to-ground distance, z/R	0.5, 1

The measurement plane was illuminated by a dual-cavity Nd:YAG laser (Quantel Evergreen, EVG00200), which delivers 200 mj per pulse. A combination of spherical and cylindrical lenses was employed to form a 2 mm light sheet to compensate for the out-of-plane motion in the z-direction. The image pairs were recorded at a rate of 15 Hz, and the time difference between the frames was set to 110 µs. Table 3 summarizes the operating conditions. For each measurement, a total of 1,000 uncorrelated image pairs were collected. The flow was seeded with fog particles having a mean diameter of 1µm and generated by a SAFEX smoke machine (SAFEX-Inside-Nebelfluid). The signal-to-noise ratio of the recorded images was improved by subtracting the overall minimum in DaVis 10.2 (LaVision GmbH) [29]. The velocity fields were then obtained through the stereoscopic multi-pass cross-correlation algorithm with a final interrogation window of 16 px × 16 px (2.4 mm × 2.4 mm) at 75 % overlap. Spurious vectors were removed and replaced in DaVis 10.2 using universal outlier detection [30] and bilinear interpolation, respectively.

4. Rotor thrust performance in ground proximity

This section provides results of the thrust performance of coaxial rotors operating close to the ground under different conditions. Two factors are evaluated: the influence of rotor speed variation and the effect of changing the axial distance between the rotors.

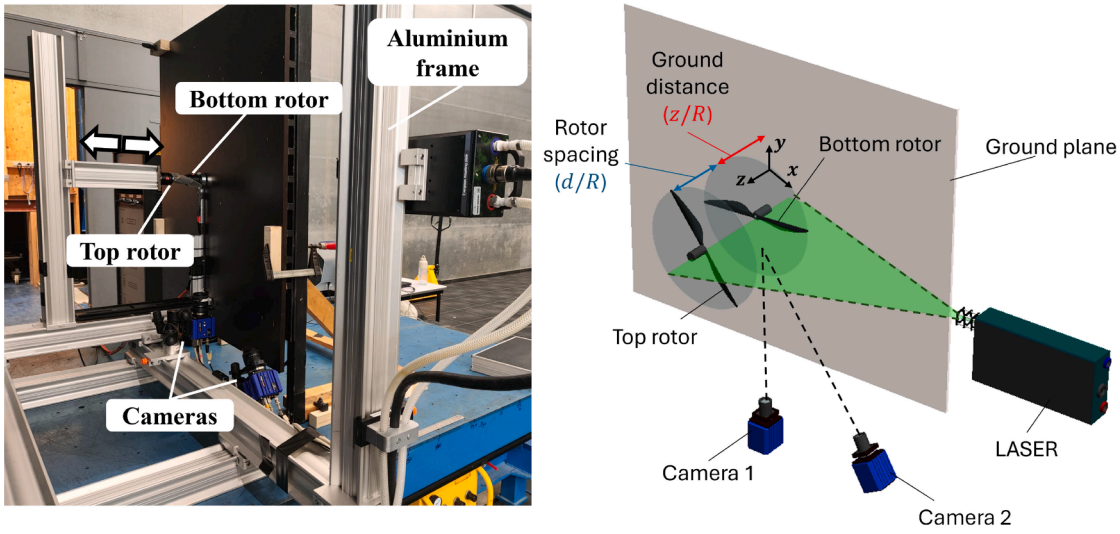

Fig. 5. Experimental setup for the PIV system. The left image shows the actual setup, including the experimental apparatus and the custom-designed frame to visualize the flow field. The right image provides a schematic representation of the system, showing the propeller spacing, the ground distance, and the field of view.

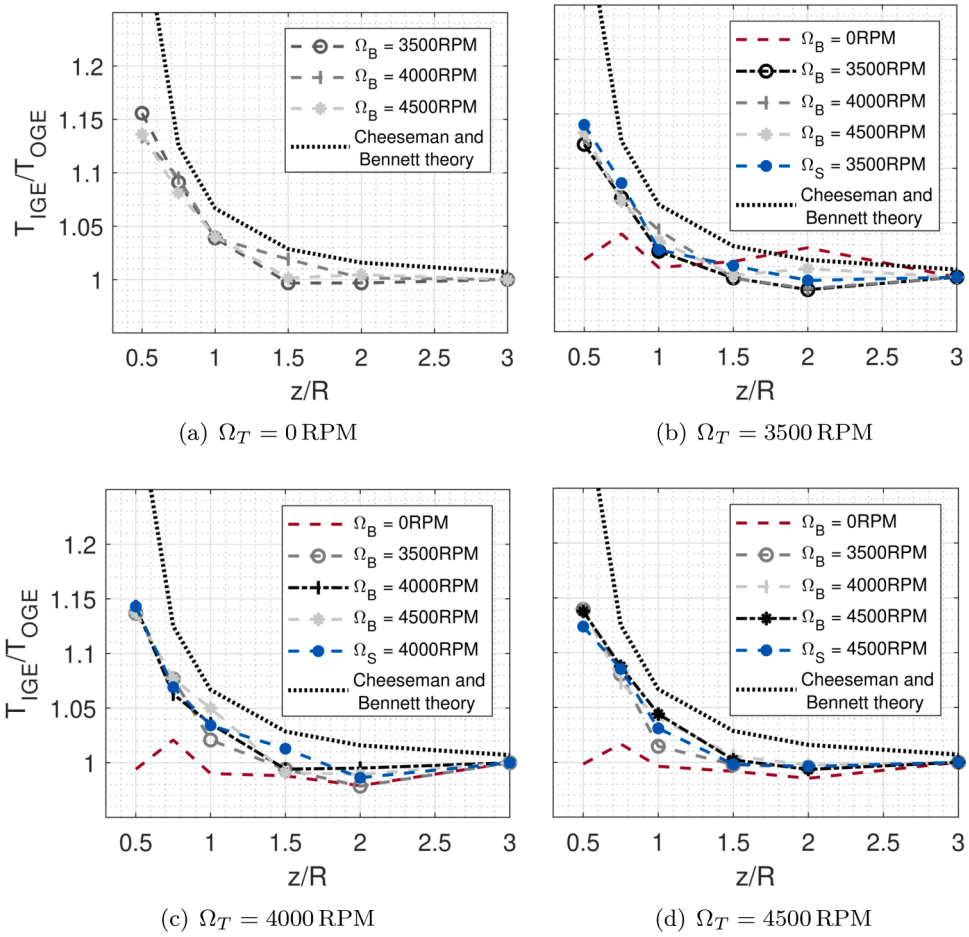

(a) $\Omega_T = 0\,\mathrm{RPM}$ (b) $\Omega_T = 3500\,\mathrm{RPM}$

(c) $\Omega_T = 4000\,\mathrm{RPM}$ (d) $\Omega_T = 4500\,\mathrm{RPM}$

Fig. 6. Thrust ratio as a function of normalized distance to the ground for a coaxial rotor system with a fixed axial separation of 0.9 R. The Cheeseman and Bennett theory is included as a reference.

4.1. Rotor speed variation in the coaxial rotor performance analysis

Fig. 6 illustrates the variation of the ground effect in coaxial rotors with fixed rotor spacing and different rotational speeds. The vertical axis in all figures represents the thrust ratio $T_{\mathrm{IGE}}/T_{\mathrm{OGE}}$, which quantifies the increase in thrust due to the ground effect, while the horizontal axis indicates the normalized distance from the bottom rotor to the ground. The axial separation between the rotors is fixed at 0.9 R, a value chosen to reflect the configuration used in a similar application by the same authors [25].

In Fig. 6(a) to (d), the speed of the top rotor (Ω_T) is held constant at 0 RPM, 3500 RPM, 4000 RPM, and 4500 RPM, respectively, while

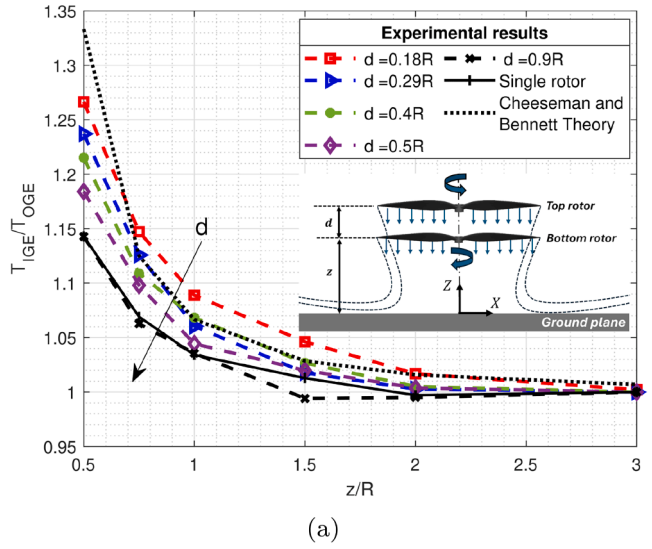

(a)

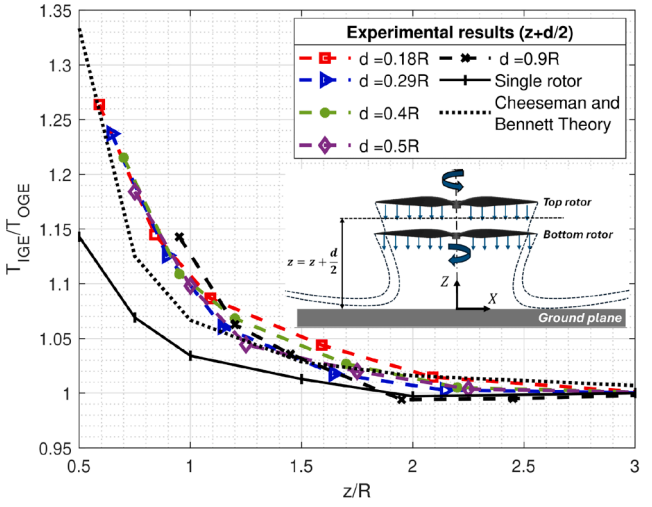

(b)

Fig. 7. Thrust ratio plotted against the normalized height above the ground for both coaxial rotors with different axial separations and a single rotor. The dashed lines represent the coaxial rotor configurations with separations ranging from $d = 0.18\,R$ to $d = 0.9\,R$, while the solid black line represents the single rotor. The dotted black line shows the Cheeseman and Bennett theory. Results are presented for two reference systems: one where z is measured from the bottom rotor to the ground (a), and another where z represents the distance from the midpoint between the rotors to the ground (b). To preserve clarity, error bars are not included in this figure, but are provided in Fig. 19.

the speed of the bottom rotor (Ω_B) is incrementally varied from 0 to 4500 RPM. The black lines highlight the case where both rotors operate at the same speed, which will be further analyzed in the following section. Additionally, the red dashed line in Fig. 6(b) and (d) shows the thrust ratio when the bottom rotor is disabled ($\Omega_B = 0$ RPM), resulting in negligible ground effects. In this situation, the top rotor behaves as a single rotor operating at an effective height of $z + d$ from the ground instead of z. The minimum height of the top rotor is 1.2 R, at which the ground effect is virtually non-existent [16].

In contrast, when the top rotor is inactive (see Fig. 6(a)), the bottom rotor is affected by the ground proximity as it lies at height z. For comparison, the thrust increase for a single rotor operating at different speeds is shown with a blue dashed line. The results illustrate that there remains minor variability in the thrust ratio with the change of

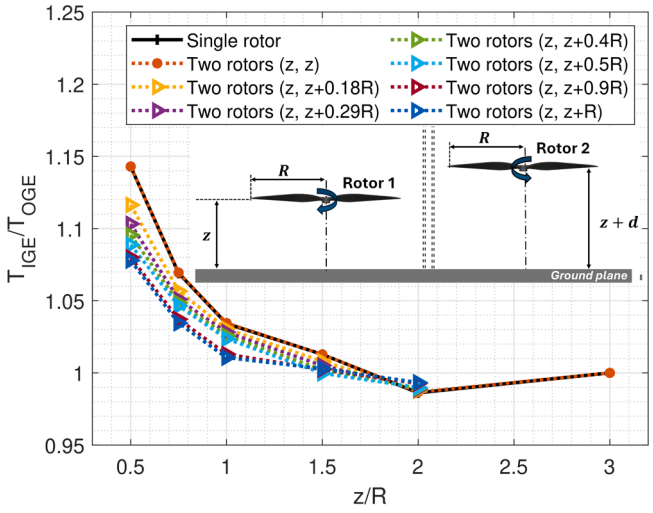

Fig. 8. Thrust ratio versus rotor height for a single rotor and two separate rotors positioned at different vertical positions relative to the ground. The solid black line represents the experimental results for a single rotor, while the dotted lines show the ground effect when two rotors are treated separately, with one placed at height z and the other at height $z + d$.

rotational speed. This indicates that, although the top rotor alters the inflow conditions of the bottom rotor, it does not lead to any changes in the ground effect. In all cases, the ground effect decreases rapidly with increasing normalized distance from the ground, becoming negligible beyond $z = 1.5\,R$. This reduction in ground effect with height is consistent with theoretical predictions and experimental observations [15]. Fig. 6 highlights that, in a coaxial rotor configuration with a fixed axial separation of 0.9 R, the ground effect is primarily dominated by the proximity of the bottom rotor to the ground. Consequently, when the rotor spacing is sufficiently large, the ground effect in the coaxial system becomes comparable to that of a single rotor.

Finally, the Cheeseman and Bennett theory is represented by black dotted lines to enable comparison with the single and coaxial configurations. Discrepancies are observed with the experimental results in both cases, particularly at shorter distances from the ground, where the ground effect is most significant. Such deviations have been widely reported by several authors in previous studies [15].

4.2. Rotor spacing effect in the coaxial rotor performance

In this section, the behavior of the coaxial rotor system is analyzed as the axial separation between the rotors is varied. As previously shown in Fig. 6, changes in rotor speeds have a minimal impact on the ground effect. Therefore, for the purposes of this analysis, both the top and bottom rotors operate at the same speed. The axial separation between the rotors affects the radial position where the inflow velocity interacts with the bottom rotor. As a result, the axial velocity distribution across the bottom rotor disk changes for each separation distance. The variation of the inflow conditions is expected to have a direct impact on the thrust generation and, consequently, the overall thrust ratio.

Fig. 7(a) presents the experimental results of the ground effect for both the coaxial rotor configuration and the single rotor, illustrating how this effect evolves as the axial separation between the rotors increases. For comparison, the Cheeseman and Bennett theory is included as a baseline. The variables z and d are defined according to the coordinate system shown in Fig. 1. In all cases, the rotors operate at a rotational speed of 4000 RPM, and the thrust ratio is plotted against the normalized height above the ground. The results highlight the influence of the rotor spacing and ground proximity on the thrust ratio.

For the coaxial configuration, smaller axial separations lead to a pronounced increase in the ground effect, particularly at lower values of

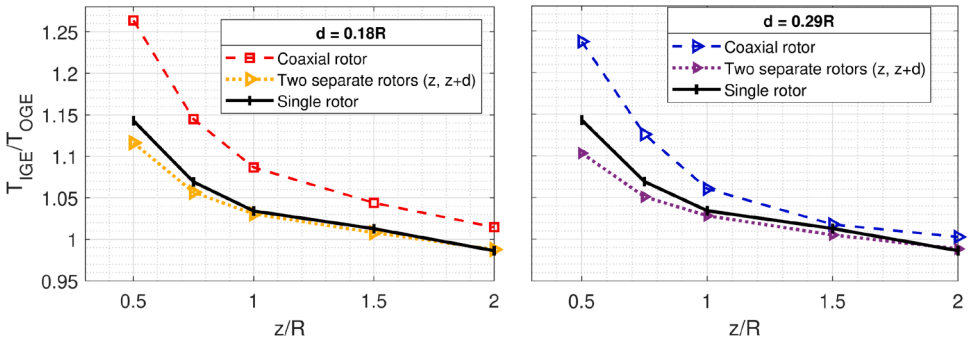

(a) $d = 0.18\,R$ (b) $d = 0.29\,R$

Fig. 9. Comparison of the ground effect for coaxial and two isolated rotors at distances of $d = 0.18\,R$ (left) and $d = 0.29\,R$ (right), illustrating the impact of rotor interaction on the ground effect. The dashed lines represent the coaxial system, while the dotted lines correspond to the two separate rotors, where no interaction occurs between them.

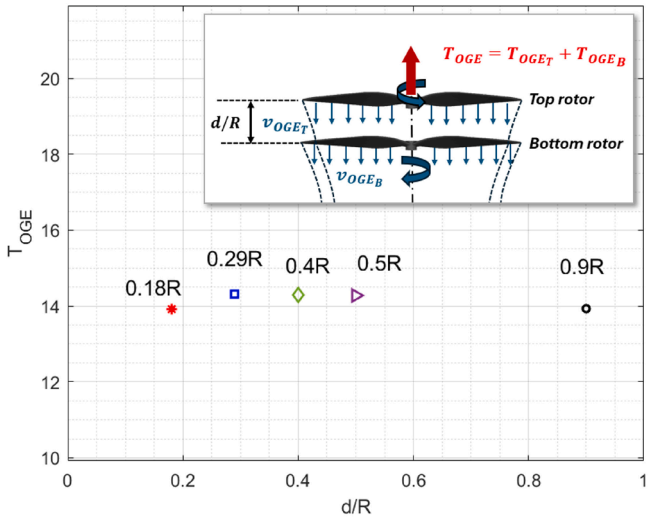

Fig. 10. Experimental variation of total thrust of the coaxial configuration under OGE conditions with normalized rotor spacing.

z/R. At $z = 0.5\,R$ and $d = 0.18\,R$, the thrust ratio increases by approximately 12 % compared to the single rotor, demonstrating the strong aerodynamic interaction between the two closely spaced rotors and the ground. This interaction arises from the induced flow generated by the top rotor, which significantly alters the inflow conditions at the bottom rotor. As the axial separation increases, the aerodynamic interaction between the rotors becomes progressively weaker. This results in a reduction of the thrust ratio, as the bottom rotor is less influenced by the incoming flow. For larger separations, such as $d = 0.9\,R$, the thrust ratio curves align closely with those of the single rotor. This trend was illustrated in Fig. 6, where, at the minimum height of the top rotor above the ground is $z = 1.2\,R$, the thrust ratio is nearly negligible. As a result, the ground effect is determined by the bottom rotor.

In all cases, the thrust ratio decreases progressively as ground proximity increases, following an exponential decay trend for all rotor spacings. Beyond $z = 1.5\,R$, the ground effect becomes negligible and the thrust ratio approaches unity, indicating a performance regime similar to OGE conditions. When these results are compared with the Cheeseman and Bennett theory, clear limitations become evident. In the case of the single rotor, a distinct discrepancy is observed between the experimental data and the theoretical prediction, an effect also reported in previous studies [15,16]. The classical theory does not account for the axial spacing between the rotors, resulting in inaccurate predictions of the thrust increase induced by the ground effect in coaxial configurations. This is particularly evident at low heights, where the ground effect is most pronounced. For example, in the case of a $d = 0.9\,R$ separation, the deviation from the theoretical prediction is 20 % at $0.5\,R$. These discrepancies highlight the inadequacy of the classical model for such configurations and emphasize the need for a more comprehensive framework tailored to coaxial rotor systems.

Fig. 7(b) presents the thrust ratio $T_{\mathrm{IGE}}/T_{\mathrm{OGE}}$ plotted with respect to the midpoint between the two rotors, for the same configurations shown in Fig. 7(a). In this case, the horizontal axis corresponds to $z = z + d/2$. This representation is equivalent to model the coaxial system as a single rotor located at the midpoint, an approach commonly adopted in previous studies where the rotor separation is very small with respect to the rotor radius [21]. In such cases, the system exhibits a near-symmetric behavior along the vertical axis.

However, in the present study, the rotor spacing is substantially larger relative to the rotor radius, which limits the applicability of the single-rotor approximation. Under the reference based on the midpoint, all thrust ratio curves converge into a single trend that aligns closely with the theoretical prediction of Cheeseman and Bennett. This convergence is the result of the geometric symmetry imposed by the midpoint definition. Nevertheless, compared to the single-rotor case, the coaxial system exhibits higher thrust levels under both ground effect and free-flight conditions. This is due to the combined thrust generated by both rotors and the aerodynamic interactions between their wakes and the ground. As the midpoint reference does not account for the physical asymmetry introduced by the rotor spacing and the ground proximity, the remainder of this study uses the position of the bottom rotor, as defined in Fig. 1.

To quantify the influence of rotor-rotor interaction on the ground effect, a non-interacting reference case is introduced. In this scenario, two identical rotors with the same geometry used as in the coaxial configuration are considered to operate independently of each other, without aerodynamic interference. Assuming a constant rotor radius, the OGE thrust is identical for both rotors. The ground effect is then given by $(T_{IGE_1} + T_{IGE_2})/(2 \cdot T_{\mathrm{OGE}})$. Fig. 8 illustrates the thrust ratio for cases where the rotors are sufficiently spaced apart and do not interact with each other. In addition, it is considered that one of the rotors is positioned at a height z and the other at a distance $z + d$ from the ground plane, where d ranges from 0 to $0.9\,R$.

The results reveal that, when the two rotors are at the same height (z and z), the ground effect is identical to that of the single rotor configuration. However, when each rotor is located at a different height (z and $z + d$), the ground effect progressively decreases as the separation d increases. This phenomenon occurs because the IGE thrust is lower at a distance $z + d$ than at a distance z. However, the OGE thrust remains unchanged in both cases. Consequently, the total thrust ratio will be lower compared to the single rotor. Overall, the absence of rotor

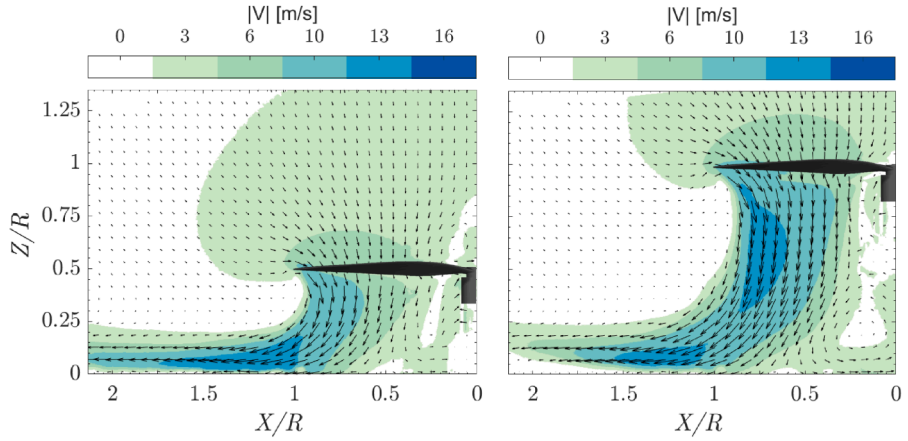

(a) $z = 0.5\,R$ (b) $z = R$

Fig. 11. Average velocity magnitude distributions for the single rotor at two vertical positions relative to the ground plane: $z = 0.5\,R$ (left) and $z = R$ (right).

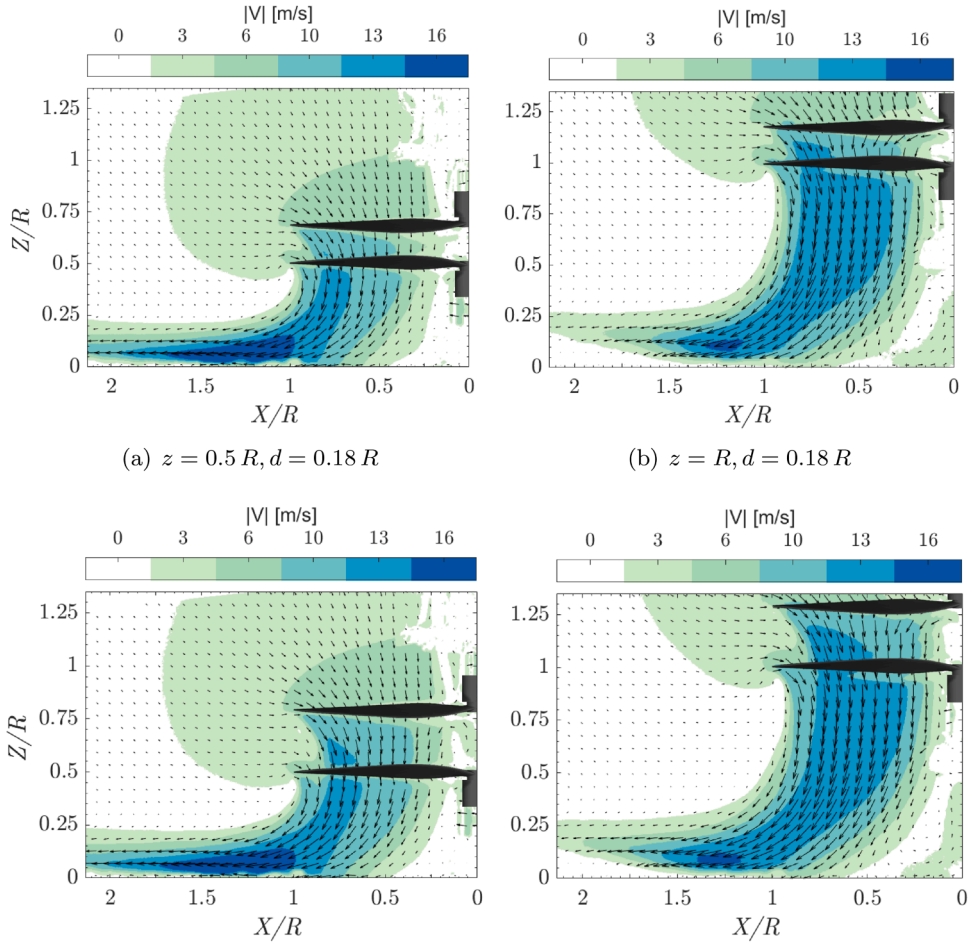

(a) $z = 0.5\,R, d = 0.18\,R$ (b) $z = R, d = 0.18\,R$

(c) $z = 0.5\,R, d = 0.29\,R$ (d) $z = R, d = 0.29\,R$

Fig. 12. Average velocity magnitude distributions for the coaxial configuration with varying rotor spacing: $d = 0.18\,R$ and $d = 0.29\,R$. Results are shown at two vertical positions relative to the ground plane: $z = 0.5\,R$ (left) and $z = R$ (right).

interaction leads to a weaker ground effect compared to the coaxial configuration.

Fig. 9 compares the ground effect of two rotors arranged in coaxial and isolated configurations for distances of $d = 0.18\,R$ and $d = 0.29\,R$. Additionally, both figures show a comparison with a single rotor. At $d = 0.18\,R$ (see Fig. 9(a)), the ground effect increases by 14.7 % in the coaxial configuration compared to the case of two isolated rotors. A similar trend is observed at $d = 0.29\,R$ (see Fig. 9(b)), where the increase is 13.4 %. In general, as the distance d increases, the discrepancy between the coaxial rotors and the two single rotors decreases. Moreover, although the ground effect diminishes when the distance d increases in both cases, the coaxial configuration consistently maintains a higher

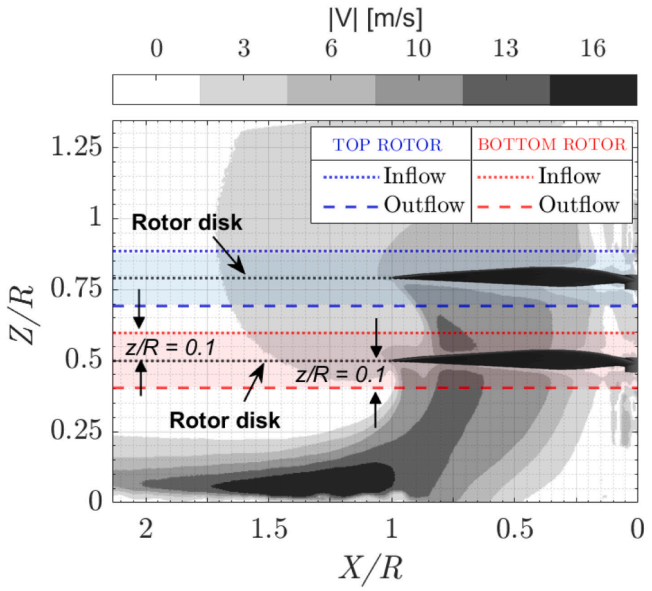

Fig. 13. Scheme illustrating where the induced velocity profile is measured for each rotor for both inflow and outflow conditions. A distance $z = \pm 0.1\ R$ with respect to the rotor disk is considered. The blue area corresponds to the top rotor and the red area to the bottom rotor. The dotted line refers to inflow conditions and the dashed line to outflow conditions. This criterion is followed in Fig. 14. (For interpretation of the references to colour in this figure legend, the reader is referred to the web version of this article.)

thrust ratio compared to the single-rotor curve. In contrast, the curves for the non-interacting rotors remain below the single-rotor curve.

However, under OGE conditions, the total thrust of the system remains nearly constant regardless of the rotor spacing, as illustrated in Fig. 10. It should be noted that this does not imply equivalent performance in terms of efficiency across different rotor spacings. These findings align with the results of Russo et al. [14] and Park et al. [13], which demonstrate that although the thrust of individual rotors varies with vertical separation, the total thrust is not affected. This contrasts sharply with IGE conditions, where rotor spacing plays a pivotal role, underscoring the significance of interactions in coaxial rotor performance. Overall, the IGE effect in coaxial configurations appears to be more pronounced than initially expected, highlighting the strong influence of the flow field on the rotors and reinforcing the impact of rotor proximity on aerodynamic behavior.

5. Time-averaged flow field visualization

This section investigates the rotor wake interactions in the coaxial configuration close to the ground through flow-field visualization. The previous section demonstrated the impact of these interactions on the ground effect, and the current analysis aims to explore the underlying physical phenomena and mechanisms responsible for these variations. Specifically, two heights above ground, $z = 0.5\ R$ and $z = R$, and two rotor spacings, $d = 0.18\ R$ and $d = 0.29\ R$, are examined. In addition, the single case is considered as a baseline. The results are depicted on a plane perpendicular to the rotor disk, illustrating the downstream evolution of the flow as it interacts with the ground plane. The single rotor and the bottom rotor in the coaxial configuration are placed at a height z above the ground, while the top rotor is positioned at a distance d above the bottom one.

Figs. 11 and 12 illustrate the time-averaged velocity distribution below the rotor in the single and coaxial configurations, respectively. In all scenarios, as the rotor approaches the ground, the interaction between its wake and the underlying surface becomes increasingly pronounced. This interaction amplifies the rotor thrust and causes the flow deflection due to the adverse pressure gradient at ground level and the flow stagnation below the rotor hub, leading to the formation of a toroidal recirculation pattern near the ground [31]. The confined space between the rotor and the ground forces the flow to expand radially as a wall jet, accelerating outward as it moves away from the central hub. This radial expansion results in a reduction in the axial velocity within the wake boundary under ground effect conditions compared to an unrestricted rotor [32].

Fig. 11(a) shows a rotor located at a distance $z = 0.5\ R$, where the averaged velocities along the wake boundary are lower than those observed in the velocity field shown in Fig. 11(b) at a distance of $z = R$. The maximum local velocities occur at the ground level, with a radial station between $x = 1\ R$ and $x = 1.7\ R$ when $z = 0.5\ R$ and $x = 1.1\ R$ to $x = 1.55\ R$ when $z = R$. Beyond these positions, the velocities decrease sharply as the wall jet reaches full development. Furthermore, the height above the wall at which this high-speed flow region is observed increases as the wall jet develops and is greater for larger wall distances. The observed trends near the ground and their progression with increasing z are consistent with findings reported in previous studies [33,34].

When comparing coaxial and single rotor configurations at the same ground distance z, coaxial rotors exhibit a higher velocity distribution. For example, Fig. 12(a) and (c) show a higher average velocity magnitude than that in Fig. 11(a) for a single rotor. In addition, a similar trend is found in the velocity field at the distance $z = R$. The interaction between the top and bottom rotor wakes significantly amplifies the ground effect compared to a single rotor. The induced flow from the top rotor modifies the inflow conditions to the bottom rotor, increasing the mass flow rate and accelerating the downstream flow. Consequently, the coaxial configuration directs a greater volume of fluid toward the ground, resulting in stronger radial expansion and higher local velocities within the wall jet. For $z = 0.5\ R$, the maximum velocity in the coaxial configuration exceeds $16\ \mathrm{m\,s^{-1}}$ at a radial station from $x = 1\ R$ to $x = 1.7\ R$. In contrast, the single rotor achieves a maximum wall jet velocity of approximately $13\ \mathrm{m\,s^{-1}}$ at $x = 1\ R$, with significantly reduced local velocities. In both cases, the velocities decrease rapidly beyond the station $x = 1.7\ R$ as the wall jet expands radially and fully develops. According to continuity principles, peak velocities along the centerline are expected to decrease inversely with distance as the wall jet fully evolves and moves away from the rotor [33]. As z increases, the overall velocity in the flow field increases, whereas the local velocities within the wall jet decrease.

The vertical separation between the rotors in the coaxial configuration determines how the streamtubes of each rotor interact with each other. This directly influences the performance and intensity of the ground effect. To assess the impact of rotor wake interactions in the coaxial configuration near the ground, the axial induced-velocity profiles under inflow and outflow conditions are analyzed. Fig. 13 presents a schematic that illustrates the position of each rotor and the distances at which the inflow and outflow conditions are measured relative to the rotor disk. The inflow condition is considered at a distance of $z = +0.1\ R$, while the outflow condition is set at $z = -0.1\ R$, following the same approach as in previous works [7,35]. Fig. 14 shows the normalized axial induced-velocity profiles (V_i/V_h) in the inflow and outflow conditions for the top and bottom rotors of the coaxial configuration when the rotor spacings are $d = 0.18\ R$ and $d = 0.29\ R$ and the heights are $z = 0.5\ R$ and $z = R$. In addition, the normalized induced velocities of the single rotor are shown as a baseline. Note that the velocity is normalized to the hover velocity of a single rotor to quantify how the interaction between the top and bottom rotor wakes is affected compared to the isolated case. For clarity of visualization, the induced velocity V_i is represented as $-V_z$, where V_z is the axial velocity component along the rotor axis.

In all cases, the V_i/V_h ratio is higher for the rotors in the coaxial configuration, as both rotors experience a flow disturbance due to their mutual presence. Moreover, it is observed that the ground effect is predominantly dominated by the bottom rotor, as it experiences the greatest

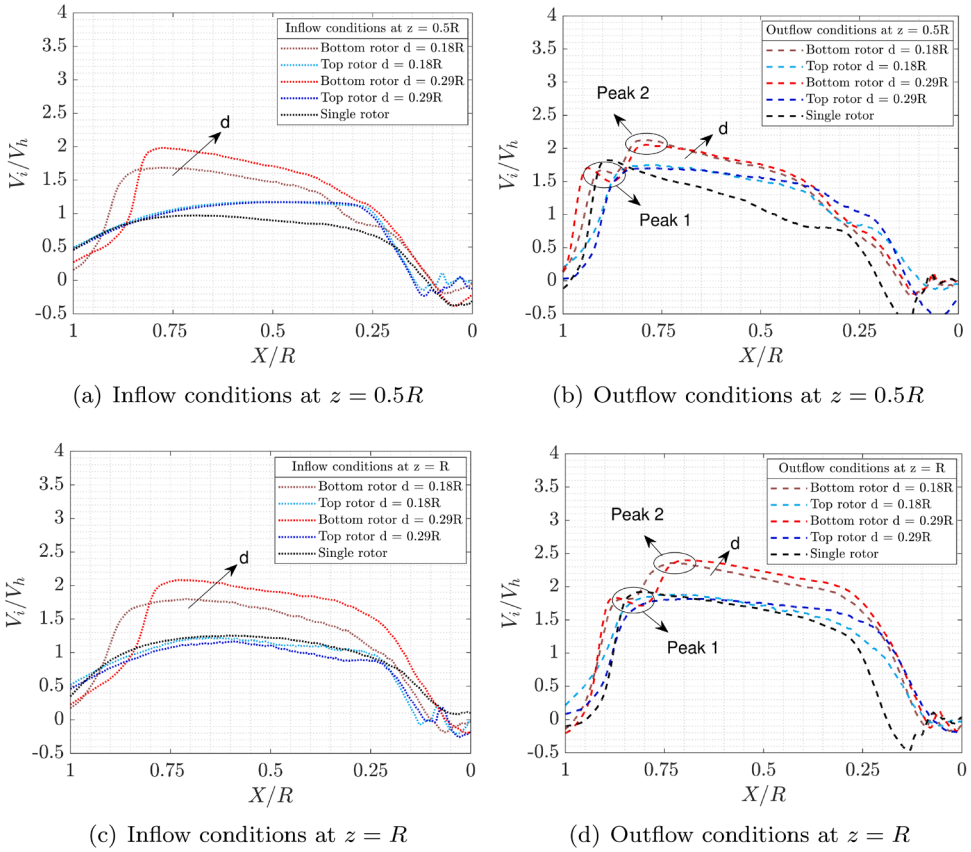

(a) Inflow conditions at $z = 0.5R$ (b) Outflow conditions at $z = 0.5R$

(c) Inflow conditions at $z = R$ (d) Outflow conditions at $z = R$

Fig. 14. Axial induced velocity normalized to the hover velocity of the single rotor. Inflow and outflow conditions are considered with respect to the disk of each rotor of the coaxial configuration. The induced velocity profiles for the single rotor are plotted as a reference.

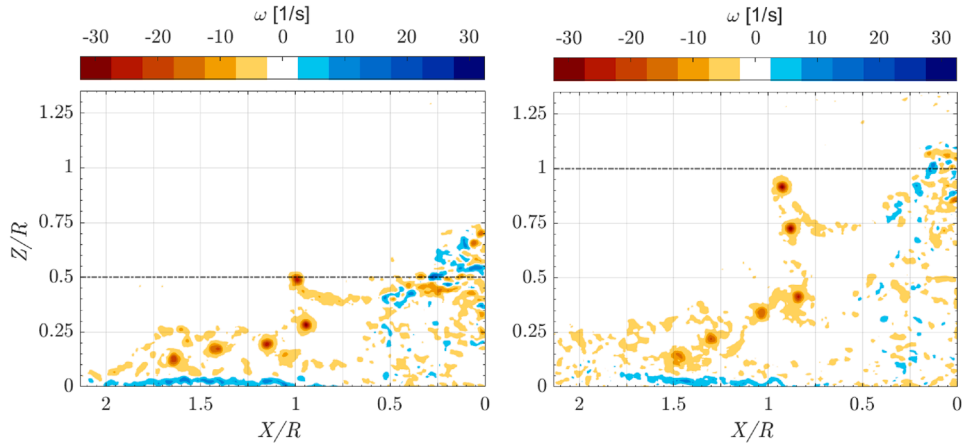

(a) $z = 0.5\,R$ (b) $z = R$

Fig. 15. Instantaneous vorticity field for the single rotor at two vertical positions relative to the ground plane: $z = 0.5\,R$ (left) and $z = R$ (right). The dotted line represents the rotor disk.

changes in induced velocity and is positioned closer to the ground. The top rotor generates downward airflow that modifies the incoming flow at the bottom rotor according to their relative position. Consequently, the bottom rotor, being in an already disturbed flow, experiences a higher inflow velocity than the top rotor, as can be seen in Fig. 14(a) and (c). As a result, the outflow velocity of the bottom rotor will also be higher (see Fig. 14(b) and (d)). When the rotor spacing increases from $d = 0.18\,R$ to $d = 0.29\,R$, the flow enters the bottom rotor more accelerated, as the wake of the top rotor has more space to develop before being accelerated by the bottom rotor, as shown in Fig. 14(a) and (c). In addition, a shift of the maximum value of V_i/V_h towards the rotor hub is observed in both the inflow and outflow conditions, with a more pronounced effect in the latter conditions. This is because as the rotor spacing increases, there is a greater radial contraction of the top rotor wake, and the region of contact of the incoming flow with the bottom rotor is delayed. These results are consistent with those shown in previous studies for unbounded coaxial rotors [7,11]. In the outflow conditions presented in Fig. 14(b) and (d), it can be observed that the normalized axial velocity of the bottom rotor exhibits two peaks, corresponding to the two flow paths generated at the tip of the blade. Peak 1 is attributed

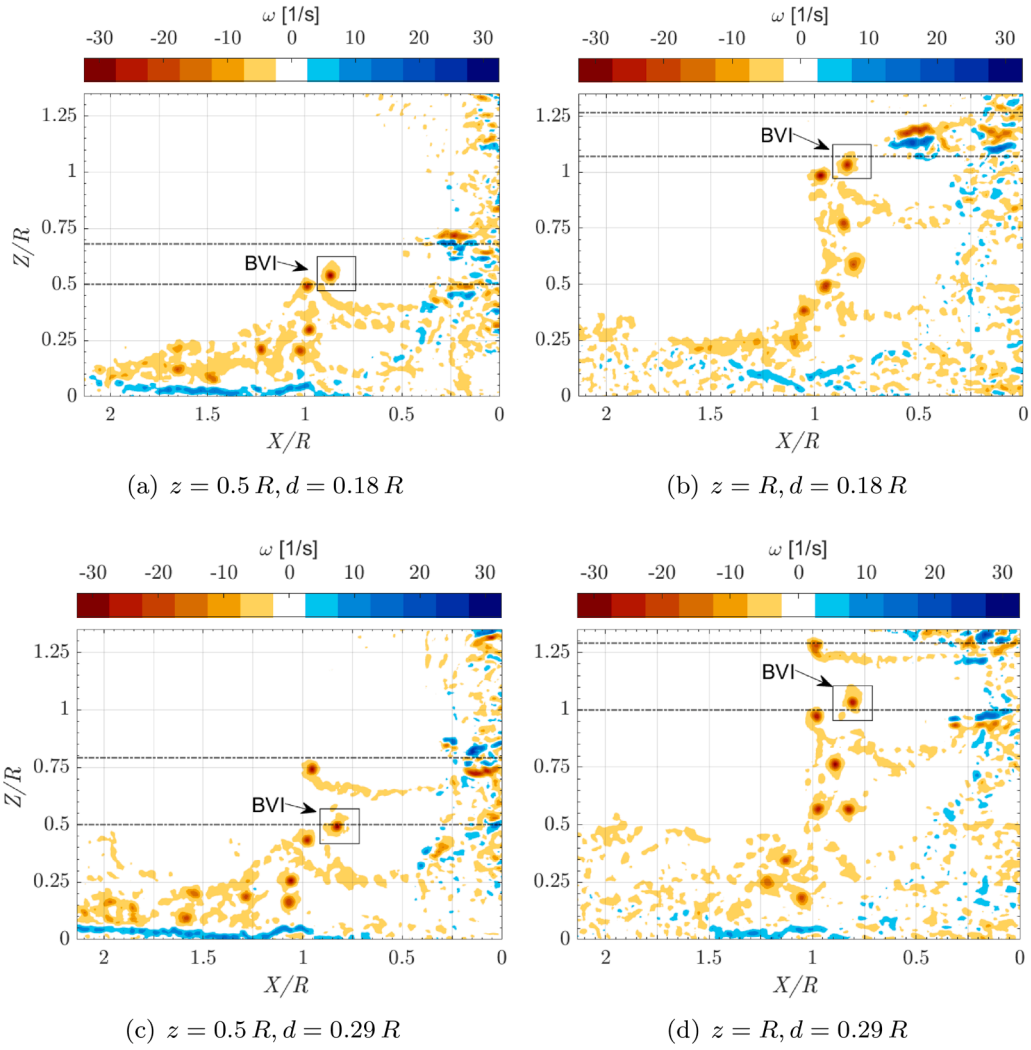

Fig. 16. Instantaneous vorticity field for the coaxial configuration with rotor separations of $d = 0.18\,R$ and $d = 0.29\,R$. The data are plotted at two heights above the ground plane: $z = 0.5\,R$ (left side) and $z = R$ (right side). The dotted line represents the top and bottom rotor disk.

to the slipstream of the bottom rotor, while Peak 2 corresponds to the slipstream of the top rotor [7].

A comparison of the two rotor heights reveals that the velocity profile trends are similar in both the inflow and outflow conditions, although the V_i/V_h ratio is higher when $z = R$. Despite the fact that the V_i/V_h ratio varies with height, the rate of change of the V_i/V_h ratio remains almost constant as the distance d increases. A higher V_i value indicates a lower reduction in the induced velocity under IGE conditions. A similar trend is observed with the rotor spacing: as the spacing increases, the influence of the ground on the bottom rotor weakens, leading to a smaller reduction in its induced velocity in both inflow and outflow regions.

Further information on the wake-ground interaction effect is obtained from the instantaneous vorticity field at different distances from the ground and rotor spacings. Fig. 15 shows the instantaneous vorticity contours for the single rotor, while Fig. 16 shows the vorticity field for the coaxial configuration. The cases under analysis are the same as those presented in the time-averaged velocity fields in Figs. 11 and 12. Figs. 15 and 16 reveal that the blade tip vortices are convected toward the ground plane along the slipstream boundary. A turbulent wall jet and a boundary layer are observed when the vortices reach the ground, resulting in the shearing of the tip vortices. For $z = 0.5\,R$ some vortices are seen in the development of the wall jet. In this case, the vortices start to disperse as they reach the ground, leading to higher local velocities and fluctuations in the ground regions. However, for $z = R$, vortex diffusion is present before reaching the ground, resulting in less pronounced velocity gradients.

In the coaxial configuration, blade-vortex interaction (BVI) occurs in the vicinity of the bottom rotor due to the wake of the top rotor interacting with the bottom rotor [11]. As previously mentioned, increasing the rotor separation leads to a greater radial reduction. This effect is evident in the position of the BVI, which is located close to the bottom rotor disk. A comparison between Fig. 16(a) and (c) and between Fig. 16(b) and (d) shows that, when the rotor spacing increases, the vortex moves closer to the rotor hub. The position of this vortex aligns with Peak 2 observed in Fig. 14(b) and (d). Additionally, for coaxial rotors, higher aperiodicity and wake instability are observed compared to the single rotor.

Analysis of velocity and vorticity fields highlights the impact of rotor interaction and ground proximity in single and coaxial configurations. The distribution of velocity and vorticity reveals consistent flow behavior as the rotor height and vertical separation are varied. Furthermore, it underscores the non-linearity of thrust variations with respect to rotor height and spacing. These findings contribute to validating the robustness of each experimental setup and confirm the reliability of the measurement procedures.

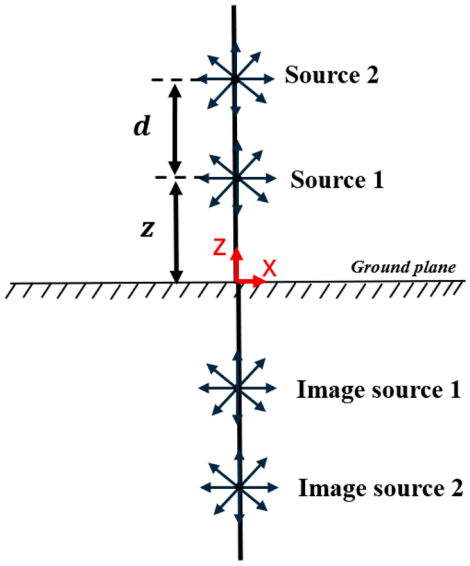

Fig. 17. Scheme of the proposed potential source model for ground effect modeling in coaxial rotors. The diagram includes the primary sources representing the coaxial rotors and their corresponding image sources relative to the ground plane.

6. Ground effect modeling

Based on analysis of performance metrics and flow field characteristics, a comprehensive model is proposed to capture the observed trends in ground proximity. This model aims to accurately predict the ground effect in coaxial rotor configurations by incorporating the combined influences of rotor spacing d and height above ground level z.

The proposed model is based on three key assumptions:

Assumption 1. Each rotor rotor is modeled as a potential source of infinitesimal extension (as from Cheeseman and Bennet [18]), as illustrated in Fig. 17. This assumption modifies Eq. (5) from Section 2 to incorporate the relative positioning of the two rotors with respect to the ground.

Assumption 2. Two sources of different strengths are used for the coaxial rotors (s_T and s_B) to physically model the interaction between the downstream wakes of the top and bottom rotors. This interaction alters the induced velocities, leading to differences in the flow field.

Assumption 3. The total power remains constant under both IGE and OGE conditions, expressed as $T_{\text{IGE}} \cdot v_{\text{IGE}} = T_{\text{OGE}} \cdot v_{\text{OGE}}$ [18]. In this context, T_{IGE} and T_{OGE} represent the combined thrust produced by the two rotors when operating in and out of ground effect, respectively.

In this framework, the bottom rotor is placed at a height z above the ground plane, while the top rotor is positioned at a distance d below the bottom rotor, as illustrated in Fig. 17. The method of images is used to satisfy the rigid boundary condition imposed by the ground, as described in Section 2.

The induced velocities of the top and bottom image rotors can be obtained by applying the definition of the potential source ϕ, as introduced in Section 2, and computing its gradient in each case. Since both rotors are aligned along the z-axis at different heights, as shown in Fig. 17, only the z-component of the velocity is considered in this configuration. The resulting expressions are:

$$\delta v_{i_T}(z,d) = \frac{s_T}{4(z+d)^2}; \tag{6}$$

$$\delta v_{i_B}(z) = \frac{s_B}{4z^2}, \tag{7}$$

where s_T and s_B denote the strengths of the top and bottom image sources, respectively, and are defined as [18]:

$$s_T = \frac{A v_{i_T}}{4\pi}; \tag{8}$$

$$s_B = \frac{A v_{i_B}}{4\pi}. \tag{9}$$

Here:

- v_{i_B} is the induced velocity at the bottom rotor, modified by the wake-induced inflow from the top rotor. It is defined as $v_{i_B} = v_{i\infty} f_B$, where $v_{i\infty}$ denotes the induced velocity of a single rotor in the unbounded environment. It serves as a reference value, representing the ideal inflow velocity in the absence of aerodynamic interactions. The factor f_B is the average reduction factor that accounts for the interference effects specific to the bottom rotor.
- v_{i_T} is the induced velocity at the top rotor, influenced by the disruption of its wake due to the presence of the bottom rotor. Similarly, it is defined as $v_{i_T} = v_{i\infty} f_T$, where f_T is the corresponding average reduction factor for the top rotor.

By combining the contributions of these potential sources and considering the different assumptions, the following expression is derived to quantify the ground effect in a coaxial configuration:

$$\left[\frac{T_{\text{IGE}}}{T_{\text{OGE}}}\right]_{(z,d)} = \frac{1}{1 - \sum_{k=1}^{n} \frac{\delta v_{i_k}}{v_{i\infty}}} = \frac{1}{1 - \frac{\delta v_{i_B}(z)}{v_{i\infty}} - \frac{\delta v_{i_T}(z,d)}{v_{i\infty}}}. \tag{10}$$

The factors f_T and f_B quantify the relative reduction in induced velocity experienced by each rotor due to mutual aerodynamic interaction. These factors are intrinsically dependent on the blade loading distribution, as any variation in the induced inflow directly alters the effective angle of attack, thereby affecting the local lift and spanwise aerodynamic loading.

In this study, the rotor geometry and the operating conditions remain constant in all configurations. Under these conditions, the inflow profiles shown in Fig. 14 exhibit a consistent overall shape across the different cases, with variations occurring primarily in magnitude and radial position. This behavior suggests that the aerodynamic loading distribution undergoes a predominantly proportional modification, which is scaled and shifted while preserving the fundamental characteristics of the distribution.

Consequently, the effect of the rotor interaction can be represented as a global scaling of the original blade loading. This supports the use of constant values for f_T and f_B, which serve as effective correction factors applied to the induced inflow. As the proposed model explicitly accounts for the rotor separation and ground proximity through the method of images, the assumption of constant coefficients is consistent with both the physical behavior of the system and the experimental observations within the tested operating envelope.

Assuming these factors to be equal to 1 implies the absence of interaction effects, treating each rotor as operating independently. Fig. 18 shows the thrust ratio using Eq. (10) with $f_T = f_B = 1$. The results indicate a substantial overestimation of the ground effect compared to the experimental data for each value of d. This discrepancy highlights the importance of accurately modeling f_T and f_B to capture the effects of mutual wake interactions, which significantly influence the reduction of induced velocities.

In the coaxial configuration, the bottom rotor, positioned closer to the ground, operates under greater flow restrictions and is significantly influenced by the wake of the top rotor. In contrast, the top rotor is located farther from the ground ($z + d$), and its inflow conditions remain unaffected. The velocity magnitude shown in Fig. 12 illustrates these differences. Fig. 14 illustrates that the interaction results in a pronounced acceleration of the inflow and outflow velocity in the bottom rotor, which deviates sharply from the single rotor baseline. In contrast,

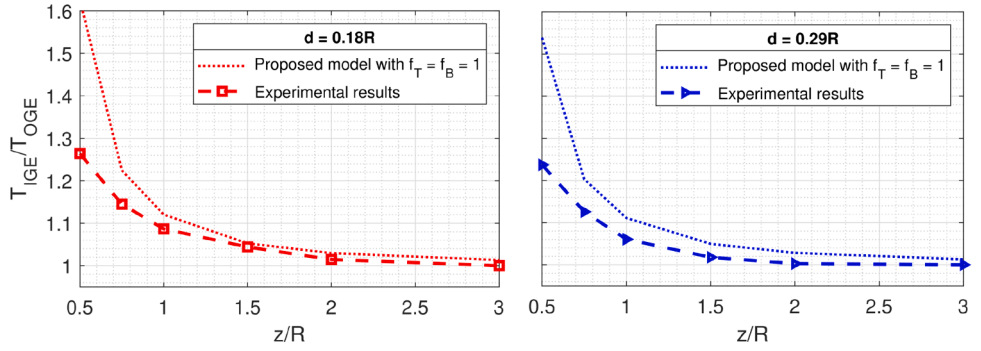

(a) $d = 0.18\,R$ (b) $d = 0.29\,R$

Fig. 18. Comparison of the proposed ground effect model with f_T and f_B set to 1, indicating no wake interaction effects, against experimental results for rotor separations of $d = 0.18\,R$ (left) and $d = 0.29\,R$ (right).

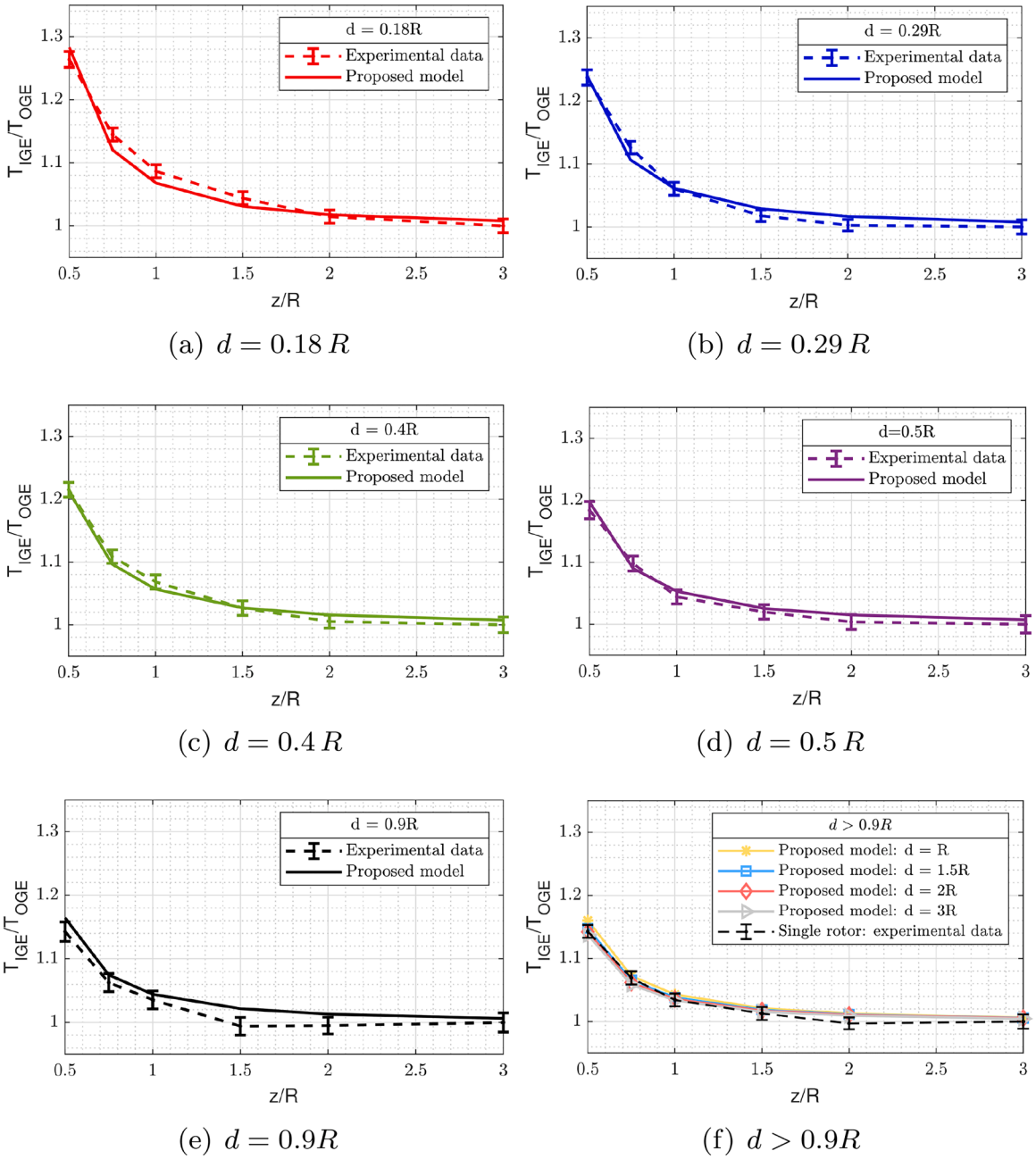

(a) $d = 0.18\,R$ (b) $d = 0.29\,R$

(c) $d = 0.4\,R$ (d) $d = 0.5\,R$

(e) $d = 0.9R$ (f) $d > 0.9R$

Fig. 19. Ground effect model predictions for the coaxial configuration, considering rotor spacings ranging from $0.18\,R$ to $0.9\,R$. The proposed model is extended to larger spacings up to $d = 3\,R$.

the top rotor shows a lower axial inflow distribution compared to the bottom rotor, mainly due to its higher ground distance $(z + d)$ and the presence of a second rotor below it. Moreover, the velocity profile of the top rotor is smoother and lacks pronounced peaks because the rotor is not subject to upstream flow disturbances. For both rotors, the induced velocity is reduced and the factors f_T, f_B must be less than 1. The reduction is more significant for the bottom rotor due to its proximity to the ground and the disturbance from the wake of the top rotor, leading to $f_B < f_T$. In view of the above, the general equation of the ground effect in coaxial rotors can be defined as

$$\left[\frac{T_{\text{IGE}}}{T_{\text{OGE}}}\right]_{(z,d)} = \frac{1}{1 - f_B \cdot \left(\frac{R}{4z}\right)^2 - f_T \cdot \left(\frac{R}{4(z+d)}\right)^2}. \tag{11}$$

The Levenberg-Marquardt algorithm [36] is used to determine the reduction factors f_T and f_B, subject to the constraints $f_B < f_T$ and $f_T, f_B < 1$. The resulting values are $f_T = 0.766, f_B = 0.467$.

Subsequently, the results of the proposed model are demonstrated against the measurements. Fig. 19 presents a comparison between the predictions of the proposed model and the experimental data. The results show a good agreement, with errors remaining below 2 % for all the tested configurations. As previously discussed, the factors f_T and f_B are tied to the blade loading distribution, which is influenced by the geometric parameters of the propeller. A commonly adopted approach to characterize this dependency is to evaluate the aerodynamic parameters at a representative radial location along the blade. In particular, the region around 75 % of the blade span tends to exhibit stable aerodynamic behavior and is often used as a reference point to estimate parameters such as the Reynolds number, the angle of attack, and the induced velocity [37]. Since the design of high-performance rotors yield comparable aerodynamic design principles, their loading distributions and inflow characteristics are expected to be similar across different geometries. However, the proposed factors may not be directly applicable to propellers with geometric characteristics significantly different to those considered in this study, e.g. significantly different disk loading or number of blades.

For this reason, it is expected that the variability of f_T and f_B will be limited when applied to rotors with similar aerodynamic and geometric properties, particularly propellers that have been specifically optimized for aerodynamic efficiency. It should also be noted that the proposed model is only applicable to steady hover conditions, which is consistent with the scope of the present study and the operational characteristics of typical drone propellers.

To further assess the applicability of the model, the coefficient of determination (R^2) is calculated by comparing the model predictions at a rotor spacing of $d = 0.9R$ with the experimental results shown in Fig. 6. These cases correspond to different combinations of rotor speeds, which inherently result in variations in blade loading, although all tests were conducted at the same spacing of $d = 0.9R$. The values obtained show consistently high agreement, with a mean R^2 of 0.87, a standard deviation of 0.05. In addition, the values of R^2 range from 0.78 to 0.95. These results indicate that, despite changes in blade loading, the model remains accurate and robust. This supports the assumption that, for propellers with similar aerodynamic characteristics and operating within the same geometric configuration, the proposed correction methodology remains valid and effective.

It is important to note that the coefficients f_T and f_B are determined using rotor spacings ranging from $0.18\,R$ to $0.9\,R$. However, Fig. 19(f) demonstrates that the model remains valid for rotor separations greater than $d > 0.9\,R$. Experimental results revealed that, for rotor separations beyond $d = 0.9\,R$, the ground effect in the coaxial rotor system becomes nearly identical to that of a single rotor. The proposed model is consistent with this observation, accurately predicting that, as the rotor separation increases further (up to $d = 3\,R$), the ground effect converges to that of a single rotor. This trend supports the hypothesis that, beyond a critical separation, the aerodynamic interaction between the rotors becomes negligible, leading to system behavior dominated by individual rotor effects.

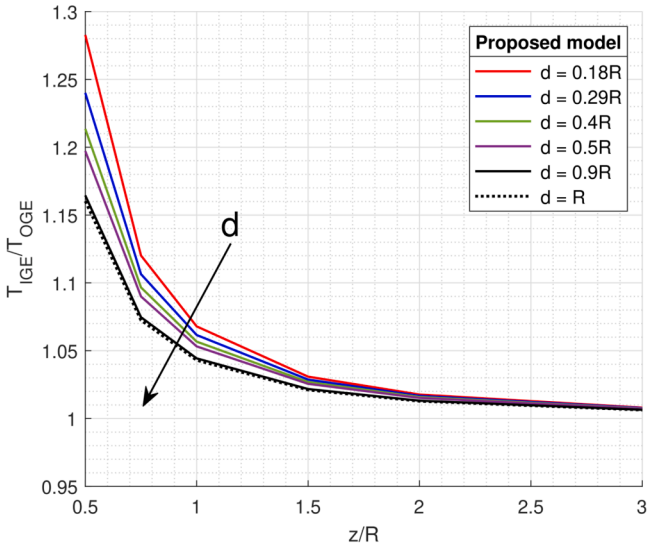

Fig. 20. Descending trend of ground effect as the rotor spacing increases. For spacings greater than $d = R$, the ground effect becomes equivalent to that of a single rotor.

Finally, Fig. 20 highlights the overall trend of the ground effect as the rotor spacing increases. This trend aligns with the results shown in Fig. 7(a), clearly illustrating an increase in the ground effect of approximately 12 % when comparing the rotor spacing closest to the single-rotor configuration. This consistent trend reinforces the robustness of the model in capturing the gradual reduction in rotor-to-rotor interaction as the rotor height increases.

The proposed model extends traditional ground effect theories by explicitly incorporating rotor-to-rotor interactions and ground proximity effects. Its ability to accurately capture the transition from interaction-dominated regimes at small rotor separations to isolated behavior at large separations provides a robust framework for analyzing the aerodynamic behavior of coaxial rotor systems under various operating conditions.

7. Conclusions

A comprehensive experimental investigation is conducted to analyze the aerodynamic behavior of single and coaxial rotor systems near the ground using thrust measurements, PIV analyses, and a semi-empirical ground effect model. The results show that the ground effect is increased in the coaxial configuration compared to the single rotors. In addition, a decreasing trend in the ground effect is observed with increasing rotor spacing due to the minimization of strong interactions between the rotors. At the minimum rotor height and spacing, the thrust ratio increases by 26 %, which is 12 % higher than that of a single rotor.

The analysis highlights the critical influence of rotor-to-rotor interactions compared to treating the system as two isolated rotors. For two single rotors positioned at the same height, the thrust ratio is similar to that of a single rotor, but when at different heights, the ground effect diminished. In contrast, coaxial configurations consistently exhibit an increased ground effect, driven by a reduced induced velocity and a higher total thrust from rotor interactions. In addition, thrust measurements over a range of rotational speeds indicate that the ground effect remains nearly unchanged, demonstrating its independence from rotor speed.

The PIV analysis reveals that the interaction between the top and bottom rotor wakes directs a larger volume of flow toward the ground, further reducing the induced velocity compared to single rotors and con-

sequently increasing the total thrust. At lower bottom rotor heights and spacings, radial expansion and shear interactions intensify, resulting in higher local velocities and pronounced vorticity near the ground. As the rotor height or spacing increases, these effects diminish due to smoother inflow conditions and reduced wake interactions.

A ground effect model is developed based on the experimental results, extending the Cheeseman and Bennet theory. Since the theoretical framework does not inherently account for rotor-to-rotor interactions, correction factors are defined using insights from PIV observations and thrust measurements. Their inclusion results in satisfactory agreement between the experimental data and the model predictions. For rotor spacings greater than $d = 0.9\,R$, the ground effect in coaxial configurations converges to that of a single rotor, demonstrating excellent consistency with experimental findings.

This comprehensive approach, which combines force measurements, detailed flow field analysis, and a ground effect model, establishes a robust framework for accurately predicting the aerodynamic performance of coaxial rotors near the ground. These findings provide a reliable basis for a deeper understanding of ground proximity effects, enabling their integration into UAV control laws for safer and more stable flight operations.

For future research, a more complete characterization of the ground effect could be achieved by independently measuring both the thrust and torque for each rotor using dedicated sensors. This would enable the phenomenon to be investigated under constant-thrust conditions, complementing the current study and providing additional insight into the energy implications of rotor height and axial rotor spacing near the ground. In addition, power measurements will be incorporated to complement the current results. Additionally, the proposed ground effect model will be integrated into a real aerial platform. This would involve evaluating how a flight controller informed by the model could improve the takeoff and landing performance of coaxial UAVs, particularly in terms of energy efficiency and near-ground stability. Further analysis is also required to generalize the fitted parameters of the proposed model to rotor systems with geometries that differ significantly from those examined in this study, thereby enabling a wider applicability.

CRediT authorship contribution statement

Ambar Garofano-Soldado: Writing – review & editing, Writing – original draft, Visualization, Validation, Software, Methodology, Investigation, Formal analysis, Data curation, Conceptualization; **Daniele Ragni:** Writing – review & editing, Supervision, Software, Resources, Project administration, Methodology, Investigation, Funding acquisition, Formal analysis, Data curation, Conceptualization; **Lourenço T. Lima Pereira:** Writing – review & editing, Supervision, Software, Methodology, Investigation, Formal analysis, Conceptualization; **Riccardo Zamponi:** Writing – review & editing, Supervision, Software, Methodology, Investigation, Formal analysis, Conceptualization; **Anibal Ollero:** Writing – review & editing, Supervision, Resources, Project administration, Investigation, Funding acquisition, Conceptualization; **Guillermo Heredia:** Writing – review & editing, Supervision, Resources, Project administration, Investigation, Funding acquisition, Conceptualization.

Data availability

Data will be made available on request.

Declaration of competing interest

Ambar Garofano Soldado reports financial support was provided by University of Seville. If there are other authors, they declare that they have no known competing financial interests or personal relationships that could have appeared to influence the work reported in this paper.

Acknowledgements

The authors thank Brian Püroja for his help in designing and assembling the experimental setups and Sen Wang for his help in performing the PIV experiments. The work of Ambar Garofano-Soldado is supported by the FPI grant (PRE2019-089812) from the Ministry of Science, Innovation and Universities of the Spanish Government. This work has been supported by the projects MARTIN-Modular Aerial Robots for inspection and maintenance of insulated pipes in the process industry, funded by the Spanish State Research Agency (PID2022-143267OB-I00), SIMAR: Safe Inspection and Maintenance supporting workers with modular robots, Artificial intelligence, and augmented Reality (HORIZON-CL4-2021-101070604), and the MORASINA ERC Consolidator Grant (ERC-2023-COG HORIZON 101124038), MOdeling and Reduction of Aeroacoustics Sources of Interaction Noise in Aviation.

References

[1] M. Hassanalian, A. Abdelkefi, Classifications, applications, and design challenges of drones: a review, Prog. Aerosp. Sci. 91 (2017) 99–131. https://doi.org/10.1016/j.paerosci.2017.04.003

[2] M.K. Taylor, A balsa-dust technique for air-flow visualization and its application to flow through model helicopter rotors in static thrust, National Advisory Committee for Aeronautics technical note, NACA 1950, https://books.google.nl/books?id=WB9Z0AEACAAJ.

[3] G. Throneberry, C.M. Hocut, A. Abdelkefi, Multi-rotor wake propagation and flow development modeling: a review, Prog. Aerosp. Sci. 127 (2021) 100762. https://doi.org/10.1016/j.paerosci.2021.100762

[4] S. Darvishpoor, J. Roshanian, A. Raissi, M. Hassanalian, Configurations, flight mechanisms, and applications of unmanned aerial systems: a review, Prog. Aerosp. Sci. 121 (2020) 100694. https://doi.org/10.1016/j.paerosci.2020.100694

[5] J.K. Cornelius, Designing a coaxial quadrotor for urban air mobility, in: 10th Biennial Autonomous VTOL Technical Meeting & 10Th Annual Electric VTOL Symposium, 2023.

[6] W. Johnson, J.F. Elmore, E.B. Keen, A.T. Gallaher, G.F. Nunez, Coaxial compound helicopter for confined urban operations, in: AHS Specialists Technical Conference on Aeromechanics Design for Vertical Lift, ARC-E-DAA-TN28919, 2016.

[7] D. Shukla, N. Komerath, Drone scale coaxial rotor aerodynamic interactions investigation, J. Fluids Eng. 141 (7) (2019) 071106. https://doi.org/10.1115/1.4042162

[8] Y. Lei, Y. Bai, Z. Xu, Q. Gao, C. Zhao, An experimental investigation on aerodynamic performance of a coaxial rotor system with different rotor spacing and wind speed, Exp. Therm Fluid Sci. 44 (2013) 779–785. https://doi.org/10.1016/j.expthermflusci.2012.09.022

[9] M. Brazinskas, S.D. Prior, J.P. Scanlan, An empirical study of overlapping rotor interference for a small unmanned aircraft propulsion system, Aerospace 3 (4) (2016). https://www.mdpi.com/2226-4310/3/4/32.

[10] M. Ramasamy, Hover performance measurements toward understanding aerodynamic interference in coaxial, tandem, and tilt rotors, J. Am. Helicopter Soci. 60 (2015). https://doi.org/10.4050/JAHS.60.032005

[11] J. Ko, S. Lee, Numerical investigation of inter-rotor spacing effects on wake dynamics of coaxial rotors, J. Aircr. 58 (2) (2021) 363–373. https://doi.org/10.2514/1.C035857

[12] D. Shukla, N. Hiremath, N.M. Komerath, Low Reynolds number aerodynamics study on coaxial and quad-rotor, 2018 Applied Aerodynamics Conference (2018). https://doi.org/10.2514/6.2018-4118

[13] S.H. Park, O.J. Kwon, Numerical study about aerodynamic interaction for coaxial rotor blades, Int. J. Aeronaut. Space Sci. 22 (2) (2021) 277–286. https://doi.org/10.1007/s42405-020-00310-6

[14] N. Russo, A.D. Marano, G.M. Gagliardi, M. Guida, T. Polito, F. Marulo, Thrust and noise experimental assessment on counter-rotating coaxial rotors, Aerospace 10 (6) (2023). https://doi.org/10.3390/aerospace10060535

[15] A. Matus-Vargas, G. Gómez, J. Martinez-Carranza, Ground effect on rotorcraft unmanned aerial vehicles: a review, Intell. Serv. Rob. 14 (2021) 1–20. https://doi.org/10.1007/s11370-020-00344-5

[16] A. Garofano-Soldado, P.J. Sanchez-Cuevas, G. Heredia, A. Ollero, Numerical-experimental evaluation and modelling of aerodynamic ground effect for small-scale tilted propellers at low Reynolds numbers, Aerosp. Sci. Technol. 126 (2022) 107625. https://doi.org/10.1016/j.ast.2022.107625

[17] X. Kan, J. Thomas, H. Teng, H.G. Tanner, V. Kumar, K. Karydis, Analysis of ground effect for small-scale UAVs in forward flight, IEEE Rob. Autom. Lett. 4 (4) (2019) 3860–3867. https://doi.org/10.1109/LRA.2019.2929993

[18] I. Cheeseman, W. Bennett, The effect of ground on a helicopter rotor in forward flight, ARC R& M 3021 (1955).

[19] P. Sanchez-Cuevas, G. Heredia, A. Ollero, Characterization of the aerodynamic ground effect and its influence in multirotor control, Int. J. Aerosp. Eng. (2017). https://doi.org/10.1155/2017/1823056

[20] A. Garofano-Soldado, A. Gonzalez-Morgado, G. Heredia, A. Ollero, Assessment and modeling of the aerodynamic ground effect of a fully-actuated hexarotor with tilted propellers, IEEE Rob. Autom. Lett. 9 (2) (2024) 1907–1914. https://doi.org/10.1109/LRA.2024.3350975

[21] L. Silwal, M. Bhagwat, V. Raghav, Aerodynamic interactions of counter-rotating coaxial rotors hovering in ground effect, J. Aircr. 59 (6) (2022) 1416–1425. https://doi.org/10.2514/1.C036941
[22] H. Zhu, S. Wei, H. Nie, Y. Du, X. Wei, Ground effect on the thrust performance of staggered rotor system, Drones 8 (4) (2024). https://doi.org/10.3390/drones8040118
[23] W. Johnson, Helicopter Theory, Courier Corporation, 2012.
[24] R. Zamponi, G. Gioli Torrione, V. Zubek, E. Gallo, A. Zarri, C. Schram, Maneuvering drone noise investigation in a reverberant environment, J. Acoust. Soc. Am. 157 (6) (2025) 4468–4481. Publisher: Acoustical Society of America (ASA). https://doi.org/10.1121/10.0036900
[25] L. Lima Pereira, B. Puroja, R. Zamponi, I. Rosa, D. Ragni, Aeroacoustic measurements of a contra-rotating UAV vehicle, Inter-Noise Noise-Con Congress Conf. Proce. (2023) 4996–5995. https://doi.org/10.3397/IN_2023_0733
[26] M. Merchant, L.S. Miller, Propeller performance measurement for low Reynolds number UAV applications, 44th AIAA Aerosp. Sci. Meeting Exhibit (2012). https://doi.org/10.2514/6.2006-1127
[27] H.J. Alons, OJF external balance. documentation NLR-CR-2008-695„ Nat. Aerosp. Lab. NLR (2008).
[28] B. Wieneke, Stereo-PIV using self-calibration on particle images, Exp. Fluids 39 (2005) 267–280.
[29] M. Raffel, C.E. Willert, F. Scarano, C.J. Kähler, S.T. Wereley, J. Kompenhans, Particle Image Velocimetry: a Practical Guide, springer, 2018.
[30] J. Westerweel, F. Scarano, Universal outlier detection for PIV data, Exp. Fluids 39 (2005) 1096–1100.
[31] E.A. Fradenburgh, The helicopter and the ground effect machine, J. Am. Helicopter Soci. 5 (4) (1960) 24–33.
[32] H.N.J. Dekker, D. Ragni, W.J. Baars, F. Scarano, M. Tuinstra, Aerodynamic interactions of side-by-side rotors in ground proximity, AIAA J. 60 (7) (2022) 4267–4277.
[33] T.E. Lee, J.G. Leishman, M. Ramasamy, Fluid dynamics of interacting blade tip vortices with a ground plane, J. Am. Helicopter Soci. 55 (2) (2010) 022005. https://doi.org/10.4050/JAHS.55.022005
[34] W.U. Zhenlong, T. ZHANG, H. TAN, H. ZHOU, W. CHEN, M. XIE, Hovering rotor aerodynamics in extreme ground effect, Chin. J. Aeronaut. 37 (7) (2024) 204–219. https://doi.org/10.1016/j.cja.2024.02.020
[35] S. Chae, S. Lee, J. Kim, Effects of rotor–rotor interaction on the wake characteristics of twin rotors in axial descent, J. Fluid Mech. 952 (2022) A31.
[36] A. Hemmati-Sarapardeh, A. Larestani, M. Nait Amar, S. Hajirezaie, Chapter 3 - training and optimization algorithms, in: A. Hemmati-Sarapardeh, A. Larestani, M. Nait Amar, S. Hajirezaie (Eds.), Applications of Artificial Intelligence Techniques in the Petroleum Industry, Gulf Professional Publishing, 2020, pp. 51–78. https://doi.org/10.1016/B978-0-12-818680-0.00003-5
[37] R. Deters, G. Ananda, M. Selig, Reynolds number effects on the performance of small-scale propellers, 2014. https://doi.org/10.2514/6.2014-2151